QCD corrections to hadronic $W\gamma$ production with nonstandard $WW\gamma$ couplings

U. Baur

Department of Physics, Florida State University, Tallahassee, Florida 32306

T. Han

Fermi National Accelerator Laboratory, P.O. Box 500, Batavia, Illinois 60510

J. Ohnemus

Department of Physics, University of Durham, Durham, DH1 3LE, England

The process $p\overset{(-)}{p} \to W^{\pm}\gamma + X \to \ell^{\pm}\nu\gamma + X$ is calculated to $O(\alpha_s)$ for general CP-conserving $WW\gamma$ couplings. At the Fermilab Tevatron center-of-mass energy, the QCD corrections to $W\gamma$ production are modest, and the Born and inclusive $O(\alpha_s)$ cross sections have similar sensitivities to the effects of anomalous couplings. At supercollider energies, the inclusive QCD corrections are large at high photon transverse momenta, reducing the sensitivity to nonstandard $WW\gamma$ couplings by up to a factor 2. The size of the QCD corrections can be reduced significantly, and a large fraction of the sensitivity lost can be regained, if a jet veto is imposed.

I. INTRODUCTION

The electroweak standard model (SM) based on an $\mathrm{SU(2)} \otimes \mathrm{U(1)}$ gauge theory has been remarkably successful in describing contemporary high energy physics experiments. The three vector boson couplings predicted by this non-Abelian gauge theory, however, remain largely untested. The production of $W\gamma$ pairs at hadron colliders provides an excellent opportunity to study the $WW\gamma$ vertex [1, 2]. In addition, the reaction $p\overset{(-)}{p} \to W^{\pm}\gamma$ is of special interest due to the presence of a zero in the amplitude of the parton level subprocess $q_1\bar{q}_2 \to W\gamma$ [3]. This phenomenon may make it possible to measure the magnetic dipole moment and electric quadrupole moment of the W boson [4, 5]. In the SM, the $WW\gamma$ vertex is completely fixed by the $\mathrm{SU(2)} \otimes \mathrm{U(1)}$ gauge structure of the electroweak sector. A measurement of the $WW\gamma$ vertex thus provides a stringent test of the SM.

In contrast with low energy data and high precision measurements at the Z peak, collider experiments offer the possibility of a direct, and essentially model independent, determination of the three vector boson vertices. Hadronic production of $W\gamma$ pairs was first calculated in Ref. [1]. The $O(\alpha_s)$ QCD corrections to the reaction $p\overset{(-)}{p} \to W^{\pm}\gamma$ were first evaluated in Ref. [6]. $O(\alpha_s^2)$ QCD corrections in the soft-plus-virtual gluon approximation were recently estimated in Ref. [7]. Studies on the potential for probing the $WW\gamma$ vertex have been performed for e^+e^- [8], ep [9], and $p\overset{(-)}{p}$ [5, 10–12] collisions. A general discussion of nonstandard model couplings of the W boson has been given in Ref. [10]. The first experimental observation of $W\gamma$ production in hadronic collisions has recently been reported by the UA2 Collaboration [13].

Previous studies on probing the $WW\gamma$ vertex via hadronic $W\gamma$ production have been based on leading-order (LO) calculations [5, 10–12]. In general, the inclu-

sion of anomalous couplings at the $WW\gamma$ vertex yields enhancements in the $W\gamma$ cross section, especially at large values of the photon transverse momentum $p_T(\gamma)$ and at large values of the $W\gamma$ invariant mass $M_{W\gamma}$ [5, 10–12]. A recent next-to-leading-order (NLO) calculation of hadronic $W\gamma$ production [14] has shown that the $O(\alpha_s)$ corrections are large in precisely these same regions. Furthermore, higher order corrections and anomalous couplings both destroy the amplitude zero of the lowest order process. It is thus vital to include the NLO corrections when using hadronic $W\gamma$ production to test the $WW\gamma$ vertex for anomalous couplings.

In this paper we calculate hadronic $W\gamma$ production to $O(\alpha_s)$, including the most general, CP-conserving, anomalous $WW\gamma$ couplings. We also include the leptonic decay of the W boson in the narrow width approximation in our calculation. In this approximation, diagrams where the photon is radiated off the final-state lepton line are not necessary to maintain electromagnetic gauge invariance. For suitable cuts these diagrams can thus be ignored, which considerably simplifies the calculation. Our calculation, which has been performed using the Monte Carlo method for NLO calculations [15], is described in Sec. II. With this method, it is easy to calculate a variety of observables simultaneously and to implement experimental acceptance cuts in the calculation. It is also possible to compute the NLO QCD corrections for exclusive channels, e.g., $p\overset{(-)}{p} \to W\gamma + 0$ jet. Apart from anomalous contributions to the $WW\gamma$ vertex we assume the SM to be valid in our calculation. In particular, we assume the coupling of the W bosons to quarks and leptons to be given by the SM.

The results of our numerical simulations are given in Sec. III. At supercollider energies, the inclusive NLO QCD corrections are very large at high photon transverse momenta in the SM. They have a severe negative impact

on the sensitivity bounds for anomalous $WW\gamma$ couplings which can be achieved at the Superconducting Super Collider (SSC) or CERN Large Hadron Collider (LHC). The large QCD corrections are caused by the combined effects of destructive interference in the Born subprocess, a log squared enhancement factor in the $q_1 g \to W\gamma q_2$ partonic cross section at high photon transverse momentum [16], and the large quark-gluon luminosity at supercollider energies. At the Fermilab Tevatron, on the other hand, the $O(\alpha_s)$ QCD corrections are found to be modest and sensitivities are only slightly affected by the QCD corrections. In Sec. III we also show that the QCD corrections at high $p_T(\gamma)$ can be significantly reduced and a large fraction of the sensitivity to anomalous couplings lost at supercollider energies can be regained, if a jet veto is imposed, i.e., if the $W\gamma + 0$ jet exclusive channel is used to extract information on the $WW\gamma$ vertex. We also find that the residual dependence of the NLO $W\gamma + 0$ jet cross section on the factorization scale Q^2 is significantly smaller than that of the $O(\alpha_s)$ cross section for the inclusive reaction $p \overset{(-)}{p} \to W\gamma + X$. Our conclusions are given in Sec. IV. Finally, there are two Appendixes containing technical details of the calculation.

II. FORMALISM

An $O(\alpha_s)$ calculation of hadronic $W\gamma$ production was recently presented in Ref. [14]. The calculation was performed for a real W boson in the final state and assumed all couplings had their standard model values. The results of Ref. [14] are extended in this section to include the leptonic decay $W \to \ell\nu$ ($\ell = e, \mu$) and anomalous (nonstandard model) couplings at the $WW\gamma$ vertex. First, the NLO Monte Carlo formalism used in this calculation is summarized and the results of Ref. [14] are outlined. These results are then generalized to include the decay $W \to \ell\nu$ and the most general CP-conserving $WW\gamma$ couplings.

The calculation is done using the narrow width approximation for the W decay. This simplifies the calculation greatly for two reasons. First of all, it is possible to ignore Feynman diagrams in which the photon is radiated off the final-state lepton line without violating electromagnetic gauge invariance. (Radiative W decay events can be suppressed by a suitable choice of cuts [11] which we will impose in our numerical simulations; see Sec. III B.) Second, in the narrow width approximation it is particularly easy to extend the NLO calculation of Ref. [14] to include the leptonic decay of the W boson.

A. Monte Carlo formalism

The NLO calculation of $W\gamma$ production includes contributions from the square of the Born graphs shown in Fig. 1, the interference between the Born graphs and the virtual one-loop graphs shown in Fig. 2, and the square of the real emission graphs shown in Fig. 3. Our calculation has been carried out using a combination of an-
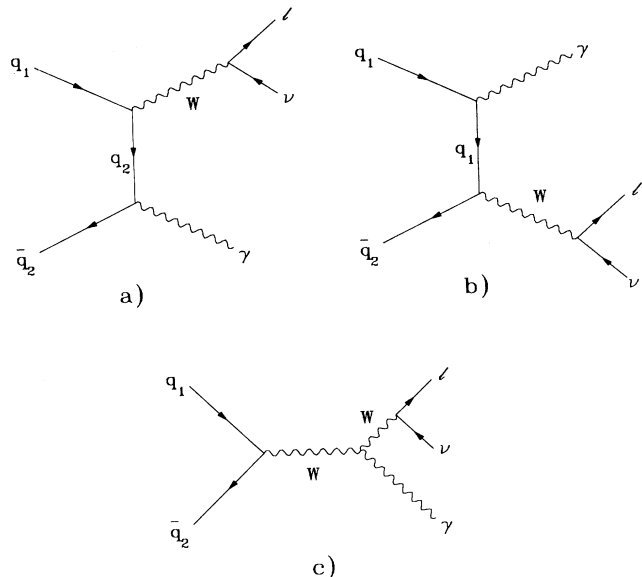

FIG. 1. Feynman diagrams for the Born subprocess $q_1 \bar{q}_2 \to W\gamma \to \ell\nu\gamma$.

alytic and Monte Carlo integration methods [15]. The basic idea is to isolate the soft and collinear singularities associated with the real emission subprocesses by partitioning phase space into soft, collinear, and finite regions. This is done by introducing theoretical soft and collinear cutoff parameters δ_s and δ_c. Using dimensional regularization [17], the soft and collinear singularities are exposed as poles in ϵ (the number of space-time dimensions is $N = 4 - 2\epsilon$ with ϵ a small number). The infrared singularities from the soft and virtual contributions are then explicitly canceled while the collinear singularities are factorized and absorbed into the definition of the parton distribution functions or the photon fragmentation functions. The remaining contributions are finite and can be evaluated in four dimensions. The Monte Carlo program thus generates n-body (for the Born and virtual contributions) and $(n+1)$-body (for the real emission contributions) final-state events. The n- and $(n + 1)$-body contributions both depend on the cutoff parameters δ_s and δ_c, however, when these contributions are added together to form a suitably inclusive observable, all dependence on the cutoff parameters cancels. The numerical results presented in this paper are insensitive to variations of the cutoff parameters; this will be demonstrated later.

B. Summary of $O(\alpha_s)$ $W\gamma$ production

The NLO cross section for hadronic $W\gamma$ production [14] consists of two- and three-body final-state contributions:

$$\sigma^{\text{NLO}}(p\overset{(-)}{p} \to W\gamma + X) = \sigma^{\text{NLO}}_{2\ \text{body}}(p\overset{(-)}{p} \to W\gamma) + \sigma_{3\ \text{body}}(p\overset{(-)}{p} \to W\gamma + X)\,. \tag{1}$$

The two-body contribution is

$$\sigma^{\text{NLO}}_{2\ \text{body}}(p\overset{(-)}{p} \to W\gamma) = \sigma^{\text{NLO}}_{\text{brem}} + \sigma^{\text{HC}} + \sum_{q_1,\bar{q}_2} \int dv\, dx_1\, dx_2$$

$$\times \left[G_{q_1/p}(x_1, M^2)\, G_{\bar{q}_2/\overset{(-)}{p}}(x_2, M^2)\, \frac{d\hat{\sigma}^{\text{NLO}}}{dv}(q_1\bar{q}_2 \to W\gamma) + (x_1 \leftrightarrow x_2) \right], \tag{2}$$

where the quantities $\sigma^{\text{NLO}}_{\text{brem}}$ and σ^{HC} are the contributions from the NLO bremsstrahlung cross section and the hard collinear remnants, respectively. These contributions are defined in Appendixes A and B, respectively, for the case of $W\gamma$ production with leptonic decay of the W boson. In Eq. (2), the sum is over all contributing quark flavors, v is related to the center-of-mass scattering angle θ^* by $v = \frac{1}{2}(1 + \cos\theta^*)$, x_1 and x_2 are the parton momentum fractions, $G_{q/p}(x, M^2)$ is a parton distribution function, M^2 is the factorization scale, and

$$\frac{d\hat{\sigma}^{\text{NLO}}}{dv}(q_1\bar{q}_2 \to W\gamma) = \frac{d\hat{\sigma}^{\text{Born}}}{dv}(q_1\bar{q}_2 \to W\gamma) \left[1 + C_F \frac{\alpha_s(\mu^2)}{2\pi} \left\{ 4\ln(\delta_s)^2 + 3\ln\left(\frac{s}{M^2}\right) + 4\ln(\delta_s)\ln\left(\frac{s}{M^2}\right) \right. \right.$$

$$\left. \left. + \lambda_{\text{FC}}\left(9 + \frac{2}{3}\pi^2 + 3\ln(\delta_s) - 2\ln(\delta_s)^2\right) \right\} \right]$$

$$+ \frac{d\hat{\sigma}^{\text{virt}}}{dv}(q_1\bar{q}_2 \to W\gamma)\,. \tag{3}$$

Here $C_F = \frac{4}{3}$ is the quark-gluon vertex color factor, $\alpha_s(\mu^2)$ is the strong running coupling evaluated at the renormalization scale μ^2, δ_s is the soft cutoff parameter, and λ_{FC} specifies the factorization convention: $\lambda_{\text{FC}} = 0$ for the universal [modified minimal subtraction $(\overline{\text{MS}})$ [18]] convention and $\lambda_{\text{FC}} = 1$ for the physical [deep inelastic scattering (DIS)] convention.

The $O(\alpha_s)$ virtual contribution to the $q_1\bar{q}_2 \to W\gamma$ cross section is

$$\frac{d\hat{\sigma}^{\text{virt}}}{dv}(q_1\bar{q}_2 \to W\gamma) = C_F\, \frac{\alpha_s(\mu^2)}{2\pi}\, \frac{1}{4}\frac{1}{9}\, \frac{(s - M_W^2)}{16\pi s^2}\, N_C\, e^4\, \frac{|U_{q_1q_2}|^2}{2x_W}\, \frac{(Q_1 t + Q_2 u)}{t + u} \left[Q_1 F^W(t, u) + Q_2 F^W(u, t) \right], \tag{4}$$

where

$$F^W(t, u) = 4\left[2\frac{s^2}{tu} + 2\frac{s}{u} + \frac{t}{u} \right] H(t, u) - \frac{8}{3}\pi^2 \frac{s}{t+u}\left[2\frac{s}{t} + \frac{t}{s} - \frac{u}{s} \right]$$

$$+ 4\left[16 - 16\frac{u}{t+u} - 16\frac{s^2}{u(t+u)} - 17\frac{s}{u} - \frac{t}{u} + 2\frac{s}{t+u} + \frac{s}{s+t} \right]$$

$$- 4\ln\left(\frac{s}{M_W^2}\right)\left[3\frac{t}{u} + 2\frac{s}{u} + 4\frac{s}{u}\frac{(t+s)}{(t+u)} + 2\frac{t}{u}\frac{s^2}{(t+u)^2} \right] + 4\ln\left(\frac{-u}{M_W^2}\right)\left[\frac{4s+u}{s+t} + \frac{su}{(s+t)^2} \right], \tag{5}$$

and

$$H(t, u) = \pi^2 - \ln\left(\frac{s}{M_W^2}\right)^2 + \ln\left(\frac{-u}{s}\right)^2 - \ln\left(\frac{-u}{M_W^2}\right)^2 - 2\,\text{Li}_2\left(1 - \frac{s}{M_W^2}\right) - 2\,\text{Li}_2\left(1 - \frac{u}{M_W^2}\right). \tag{6}$$

The W-boson mass is denoted by M_W, $N_C = 3$ is the number of colors, e is the electromagnetic coupling constant, $U_{q_1q_2}$ is the Cabibbo-Kobayashi-Maskawa quark mixing matrix, $x_W = \sin^2\theta_W$ where θ_W is the weak mixing angle, and Q_1 and Q_2 are the electric charges of q_1 and q_2 in units of the proton charge e. The $2 \to 2$ subprocess is labeled by $q_1(p_1) + \bar{q}_2(p_2) \to W(p_3) + \gamma(p_4)$ and the parton level kinematic invariants s, t, u are defined by

$$s = (p_1 + p_2)^2, \qquad t = (p_1 - p_3)^2, \qquad u = (p_1 - p_4)^2. \tag{7}$$

The function $\text{Li}_2(z)$ is the dilogarithm function

$$\text{Li}_2(z) = -\int_0^1 \ln(1 - tz)\frac{dt}{t} = \sum_{k=1}^{\infty} \frac{z^k}{k^2}. \tag{8}$$

The three-body contribution to the NLO cross section is

$$\sigma_{3\,\text{body}}(p\overset{(-)}{p} \to W\gamma + X) = \sum_{a,b,c} \int d\hat{\sigma}(ab \to W\gamma c)\Big[G_{a/p}(x_1, M^2)\, G_{b/\overset{(-)}{p}}(x_2, M^2) + (x_1 \leftrightarrow x_2)\Big]dx_1\, dx_2\,, \tag{9}$$

where the sum is over all partons contributing to the three subprocesses $q_1\bar{q}_2 \to W\gamma g$, $q_1 g \to W\gamma q_2$, and $g\bar{q}_2 \to W\gamma\bar{q}_1$. The $2 \to 3$ subprocess is labeled by $p_1 + p_2 \to p_3 + p_4 + p_5$ and the kinematic invariants s_{ij}

and t_{ij} are defined by $s_{ij} = (p_i + p_j)^2$ and $t_{ij} = (p_i - p_j)^2$. The integration over three-body phase space and $dx_1\, dx_2$ is done numerically by standard Monte Carlo techniques. The kinematic invariants s_{ij} and t_{ij} are first tested for soft and collinear singularities. If an invariant for a subprocess falls in a soft or collinear region of phase space, the contribution from that subprocess is not included in the cross section.

Except for the virtual contribution, $d\hat{\sigma}^{\text{virt}}/dv$ in Eq. (3), the $O(\alpha_s)$ corrections are all proportional to the Born cross section. It is easy to incorporate the decay $W \to \ell\nu$ into those terms which are proportional to the Born cross section; one simply replaces $d\hat{\sigma}^{\text{Born}}(q_1\bar{q}_2 \to W\gamma)$ with $d\hat{\sigma}^{\text{Born}}(q_1\bar{q}_2 \to W\gamma \to \ell\nu\gamma)$ in Eq. (3). It is likewise easy to include the W decay in the NLO bremsstrahlung, the hard collinear, and the real emission contributions by making analogous replacements. When working at the amplitude level, the W decay is trivial to implement; one simply replaces the W-boson polarization vector $\epsilon_\mu(k)$ with the $W \to \ell\nu$ decay current $J_\mu(k)$ in the amplitude. Details of the amplitude level calculations for the Born and real emission subprocesses can be found in Ref. [19].

The only term in which it is more difficult to incorporate the W decay is the virtual contribution. Rather than undertake the nontrivial task of recalculating the virtual
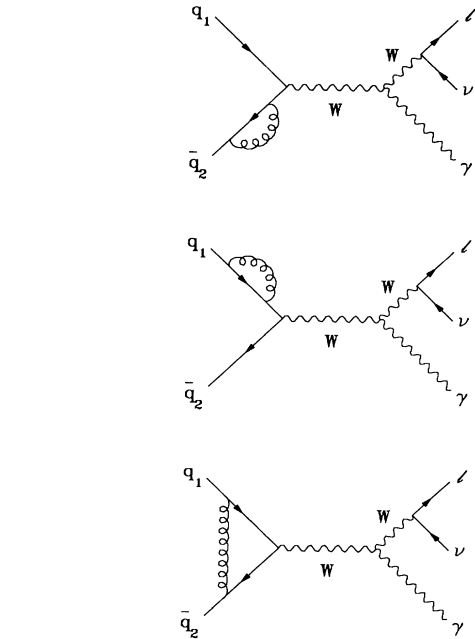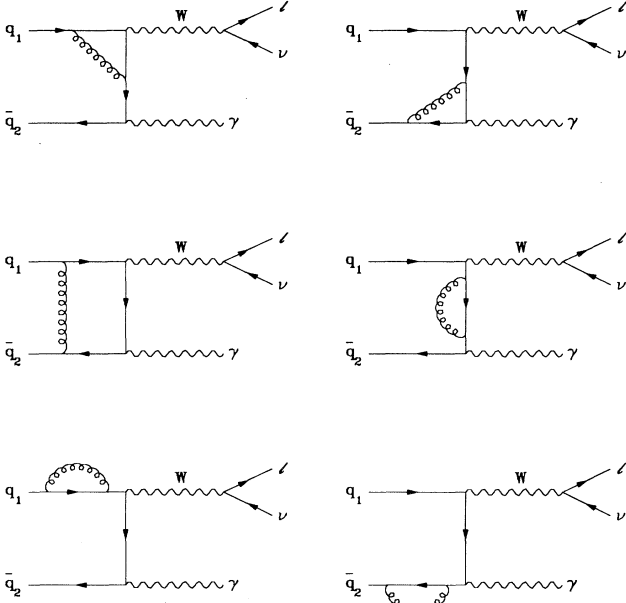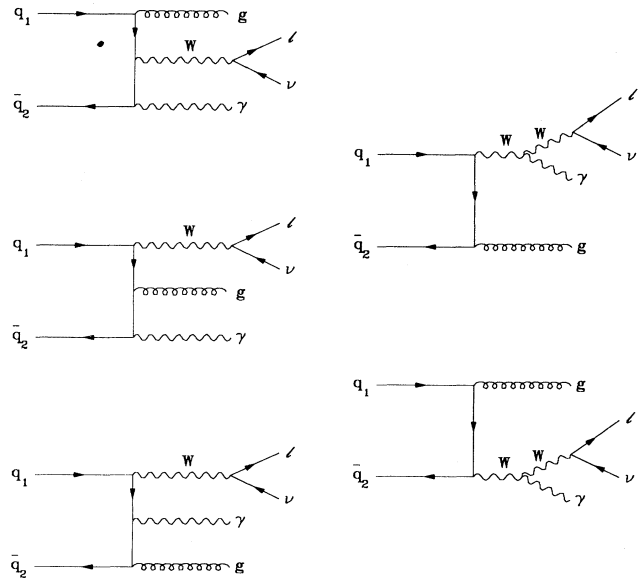

FIG. 2. Feynman diagrams for the virtual subprocess $q_1\bar{q}_2 \to W\gamma \to \ell\nu\gamma$. Not shown are the diagrams obtained by interchanging the W and γ.

FIG. 3. Feynman diagrams for the real emission subprocess $q_1\bar{q}_2 \to W\gamma g \to \ell\nu\gamma g$. Not shown are the diagrams obtained by interchanging the W and γ.

correction term for the case of a leptonically decaying W boson, we have instead opted to use the virtual correction for a real on-shell W boson which we subsequently decay ignoring spin correlations. When spin correlations are ig-

nored, the squared matrix element for W-boson production and decay factorizes into separate production and decay squared matrix elements when the sum over spins is carried out; i.e.,

$$\sum_{\text{spins}} |\mathcal{M}(q_1 \bar{q}_2 \rightarrow W + X \rightarrow \ell\nu + X)|^2 \approx \sum_{\text{spins}} |\mathcal{M}(q_1 \bar{q}_2 \rightarrow W + X)|^2 (4\pi)^2 \, B(W \rightarrow \ell\nu) \, \delta(q_{\ell\nu}^2 - M_W^2) \,, \tag{10}$$

where $B(W \rightarrow \ell\nu)$ is the $W \rightarrow \ell\nu$ branching ratio and $q_{\ell\nu}^2$ is the squared $\ell\nu$ invariant mass.

Neglecting spin correlations slightly modifies the shapes of the angular distributions of the final-state leptons. If no angular cuts (e.g., rapidity cuts) are imposed on the final-state leptons, then ignoring spin correlations does not alter the total cross section. For realistic rapidity cuts, cross sections are changed by typically 10% if spin correlations are neglected. Since the size of the virtual correction is only about 1% the size of the Born cross section, the overall effect of neglecting the spin correlations in the virtual correction is expected to be negligible compared to the 20% − 30% uncertainty from the parton distribution functions and the choice of the scale Q^2. This will be demonstrated explicitly in Sec. III D. (Note that spin correlations are included everywhere in the calculation except in the virtual contribution.)

C. Incorporation of the decay $W \rightarrow \ell\nu$

The results for the NLO calculation of $p\overset{(-)}{p} \rightarrow W^{\pm}\gamma + X \rightarrow \ell^{\pm}\nu\gamma + X$ can now be summarized. The NLO cross section now consists of three- and four-body final-state contributions:

$$\sigma^{\text{NLO}}(p\overset{(-)}{p} \rightarrow W\gamma + X \rightarrow \ell\nu\gamma + X) = \sigma_{3\,\text{body}}^{\text{NLO}}(p\overset{(-)}{p} \rightarrow W\gamma \rightarrow \ell\nu\gamma) + \sigma_{4\,\text{body}}(p\overset{(-)}{p} \rightarrow W\gamma + X \rightarrow \ell\nu\gamma + X) \,. \tag{11}$$

The three-body contribution is

$$\sigma_{3\,\text{body}}^{\text{NLO}}(p\overset{(-)}{p} \rightarrow W\gamma \rightarrow \ell\nu\gamma) = \sigma_{\text{brem}}^{\text{NLO}} + \sigma^{\text{HC}} + \sum_{q_1,\bar{q}_2} \int dv \, dx_1 \, dx_2$$

$$\times \left[G_{q_1/p}(x_1, M^2) \, G_{\bar{q}_2/\overset{(-)}{p}}(x_2, M^2) \, \frac{d\hat{\sigma}^{\text{NLO}}}{dv}(q_1 \bar{q}_2 \rightarrow W\gamma \rightarrow \ell\nu\gamma) + (x_1 \leftrightarrow x_2) \right], \tag{12}$$

where $\sigma_{\text{brem}}^{\text{NLO}}$ is the NLO bremsstrahlung cross section defined in Appendix A, σ^{HC} is the hard collinear remnant contribution defined in Appendix B, the sum is over all contributing quark flavors, and

$$\frac{d\hat{\sigma}^{\text{NLO}}}{dv}(q_1 \bar{q}_2 \rightarrow W\gamma \rightarrow \ell\nu\gamma) = \frac{d\hat{\sigma}^{\text{Born}}}{dv}(q_1 \bar{q}_2 \rightarrow W\gamma \rightarrow \ell\nu\gamma) \left[1 + C_F \frac{\alpha_s(\mu^2)}{2\pi} \left\{ 4\ln(\delta_s)^2 \right.\right.$$

$$\left.\left. + 3\ln\left(\frac{s}{M^2}\right) + 4\ln(\delta_s)\ln\left(\frac{s}{M^2}\right) + \lambda_{\text{FC}}\left[9 + \tfrac{2}{3}\pi^2 + 3\ln(\delta_s) - 2\ln(\delta_s)^2 \right] \right\} \right]$$

$$+ \frac{d\hat{\sigma}^{\text{virt}}}{dv}(q_1 \bar{q}_2 \rightarrow W\gamma) \, B(W \rightarrow \ell\nu) \,. \tag{13}$$

The virtual contribution $d\hat{\sigma}^{\text{virt}}/dv(q_1 \bar{q}_2 \rightarrow W\gamma)$, which is defined in Eq. (4), is multiplied here by the $W \rightarrow \ell\nu$ branching ratio.

The four-body contribution is

$$\sigma_{4\,\text{body}}(p\overset{(-)}{p} \rightarrow W\gamma + X \rightarrow \ell\nu\gamma + X) = \sum_{a,b,c} \int d\hat{\sigma}(ab \rightarrow W\gamma c \rightarrow \ell\nu\gamma c)$$

$$\times \left[G_{a/p}(x_1, M^2) \, G_{b/\overset{(-)}{p}}(x_2, M^2) + (x_1 \leftrightarrow x_2) \right] dx_1 \, dx_2 \,, \tag{14}$$

where the sum is over all partons contributing to the three subprocesses $q_1 \bar{q}_2 \rightarrow W\gamma g \rightarrow \ell\nu\gamma g$, $q_1 g \rightarrow W\gamma q_2 \rightarrow \ell\nu\gamma q_2$, and $g\bar{q}_2 \rightarrow W\gamma \bar{q}_1 \rightarrow \ell\nu\gamma \bar{q}_1$. The squared matrix elements for the Born subprocess and the real emission subprocesses were evaluated numerically via helicity amplitude methods as described in Ref. [19].

D. Incorporation of anomalous $WW\gamma$ couplings

The $WW\gamma$ vertex is uniquely determined in the SM by SU(2) $\otimes$ U(1) gauge invariance. In $W\gamma$ production both the virtual W and the decaying on-shell W couple to essentially massless fermions, which ensures that effectively

$\partial_\mu W^\mu = 0$. This condition together with Lorentz invariance, electromagnetic gauge invariance, and CP conservation, allows two free parameters κ and λ in the $WW\gamma$ vertex. The most general Lorentz and CP-invariant vertex compatible with electromagnetic gauge invariance is described by the effective Lagrangian [20]

$$\mathcal{L}_{WW\gamma} = -i\,e\left[W_{\mu\nu}^\dagger W^\mu A^\nu - W_\mu^\dagger A_\nu W^{\mu\nu} + \kappa W_\mu^\dagger W_\nu F^{\mu\nu} + \frac{\lambda}{M_W^2}W_{\lambda\mu}^\dagger W_\nu^\mu F^{\nu\lambda}\right],\tag{15}$$

where A^μ and W^μ are the photon and W^- fields, respectively, $W_{\mu\nu} = \partial_\mu W_\nu - \partial_\nu W_\mu$, and $F_{\mu\nu} = \partial_\mu A_\nu - \partial_\nu A_\mu$. All higher dimensional operators are obtained by replacing W^μ with $(\partial^2)^m W^\mu$, where m is an arbitrary positive integer, in the terms proportional to $\Delta\kappa = \kappa - 1$ and λ. These operators form a complete set and can be summed up by replacing $\Delta\kappa$ and λ by momentum dependent form factors. All details are contained in the specific functional form of the form factor and its scale Λ. The form factor nature of $\Delta\kappa$ and λ will be discussed in more detail later.

In Eq. (15), without loss of generality, we have chosen the W boson mass M_W as the energy scale in the denominator of the term proportional to λ. If a different mass scale $\mathbb{M}$ had been used in Eq. (15), then all of our subsequent results could be obtained by scaling λ by a factor $\mathbb{M}^2/M_W^2$.

The variables κ and λ are related to the magnetic dipole moment μ_W and the electric quadrupole moment Q_W of the W boson:

$$\mu_W = \frac{e}{2M_W}(1 + \kappa + \lambda),\tag{16}$$

$$Q_W = -\frac{e}{M_W^2}(\kappa - \lambda).\tag{17}$$

At tree level in the SM, $\kappa = 1$ and $\lambda = 0$. The two CP conserving couplings have recently been measured by the UA2 Collaboration in the process $p\bar{p} \to e^\pm\nu\gamma X$ at the CERN $p\bar{p}$ collider [13]:

$$\kappa = 1_{+2.6}^{-2.2}\ (\text{for }\lambda = 0),\qquad \lambda = 0_{+1.7}^{-1.8}\ (\text{for }\kappa = 1),\tag{18}$$

at the 68.3% confidence level (C.L.). Although bounds on these couplings can also be extracted from low energy data and high precision measurements at the Z pole, there are ambiguities and model dependencies in the results [21–23]. From loop contributions to $(g-2)_\mu$ one estimates [24] limits which are typically ~ 1 to 10. No rigorous bounds on $WW\gamma$ couplings can be obtained from data from the CERN e^+e^- collider LEP I if correlations between different contributions to the anomalous couplings are fully taken into account. Without serious cancellations among various one-loop contributions, one finds [23, 25] $|\Delta\kappa|$, $|\lambda| \le 0.5 - 1.5$ at the 90% C.L. from present data on S, T, and U [26] (or, equivalently, ϵ_1, ϵ_2, and ϵ_3 [27]). In contrast, one expects deviations from the SM of $\sim 10^{-2}$ or less for κ and λ if an approach based on chiral perturbation theory [28] is used.

If CP violating $WW\gamma$ couplings are allowed, two additional free parameters, $\tilde{\kappa}$ and $\tilde{\lambda}$ appear in the effective Lagrangian. However, CP violating operators are tightly constrained by measurements of the neutron electric dipole moment which restrict $\tilde{\kappa}$ and $\tilde{\lambda}$ to $|\tilde{\kappa}|$, $|\tilde{\lambda}| \lesssim 10^{-3}$ [29]. CP violating $WW\gamma$ couplings are, therefore, not considered in this paper.

The Feynman rule for the $WW\gamma$ vertex factor corresponding to the Lagrangian in Eq. (15) is

$$-i\,e\,(Q_1 - Q_2)\,\Gamma_{\beta\mu\nu}(k, k_1, k_2) = -i\,e\,(Q_1 - Q_2)\left[\Gamma_{\beta\mu\nu}^{\text{SM}}(k, k_1, k_2) + \Gamma_{\beta\mu\nu}^{\text{NSM}}(k, k_1, k_2)\right],\tag{19}$$

where the labeling conventions for the four-momenta and Lorentz indices are defined by Fig. 4, $(Q_1 - Q_2)$ is the electric charge of the W boson (Q_1 and Q_2 are the electric charges of q_1 and q_2 in units of the proton charge e), and the factors Γ^{SM} and Γ^{NSM} are the SM and nonstandard model vertex factors:

$$\Gamma_{\beta\mu\nu}^{\text{SM}}(k, k_1, k_2) = (k_1 - k_2)_\beta\, g_{\nu\mu} + 2\,k_\mu\, g_{\beta\nu} - 2\,k_\nu\, g_{\beta\mu},\tag{20}$$

$$\Gamma_{\beta\mu\nu}^{\text{NSM}}(k, k_1, k_2) = \frac{1}{2}\left(\Delta\kappa + \lambda\frac{k^2}{M_W^2}\right)(k_1 - k_2)_\beta\, g_{\nu\mu} - \frac{\lambda}{M_W^2}(k_1 - k_2)_\beta\, k_\nu\, k_\mu + (\Delta\kappa + \lambda)\, k_\mu\, g_{\beta\nu}.\tag{21}$$

The nonstandard model vertex factor is written here in terms of $\Delta\kappa = \kappa - 1$ and λ, which both vanish in the SM.

It is straightforward to include the nonstandard model couplings in the amplitude level calculations. Using the computer algebra program FORM [30], we have computed the $q_1\bar{q}_2 \to W\gamma$ virtual correction with the modified vertex factor of Eq. (19), however, the resulting expression is too lengthy to present here. The nonstandard $WW\gamma$ couplings of Eq. (15) do not destroy the renormalizability of QCD. Thus, the infrared singularities from the soft

and virtual contributions are explicitly canceled, and the collinear singularities are factorized and absorbed into the definition of the parton distribution and photon fragmentation functions, exactly as in the SM case.

The anomalous couplings cannot be simply inserted into the vertex factor as constants because this would violate S-matrix unitarity. Tree level unitarity uniquely restricts the $WW\gamma$ couplings to their SM gauge theory values at asymptotically high energies [31]. This implies that any deviation of $\Delta\kappa$ or λ from the SM expectation
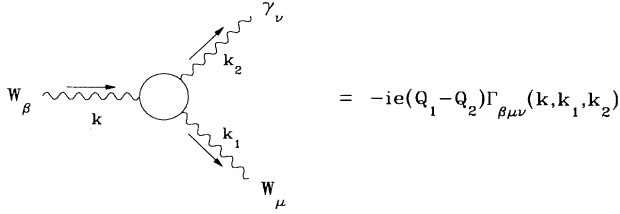
FIG. 4. Feynman rule for the general $WW\gamma$ vertex. The factor e is the electromagnetic coupling constant and $(Q_1 - Q_2)$ is the electric charge of the W boson. The vertex function $\Gamma_{\beta\mu\nu}(k, k_1, k_2)$ is given in Eq. (19).

has to be described by a form factor $\Delta\kappa(M_{W\gamma}^2, p_W^2, p_\gamma^2)$ or $\lambda(M_{W\gamma}^2, p_W^2, p_\gamma^2)$ which vanishes when either the square of the $W\gamma$ invariant mass, $M_{W\gamma}^2$, or the square of the four-momentum of the final state W or photon $(p_W^2$ or $p_\gamma^2)$ becomes large. In $W\gamma$ production $p_\gamma^2 = 0$ and $p_W^2 \approx M_W^2$ even when the finite W width is taken into account. However, large values of $M_{W\gamma}^2$ will be probed at future hadron colliders such as the LHC or the SSC and the $M_{W\gamma}^2$ dependence of the anomalous couplings has to be included in order to avoid unphysical results which would violate unitarity. Consequently, the anomalous couplings are introduced via form factors [10, 32]

$$\Delta\kappa(M_{W\gamma}^2, p_W^2 = M_W^2, p_\gamma^2 = 0) = \frac{\Delta\kappa_0}{(1 + M_{W\gamma}^2/\Lambda^2)^n},$$
(22)

$$\lambda(M_{W\gamma}^2, p_W^2 = M_W^2, p_\gamma^2 = 0) = \frac{\lambda_0}{(1 + M_{W\gamma}^2/\Lambda^2)^n},$$
(23)

where $\Delta\kappa_0$ and λ_0 are the form factor values at low energies and Λ represents the scale at which new physics becomes important in the weak boson sector, e.g., due to a composite structure of the W boson. In order to guarantee unitarity, $n > 1/2$ for $\Delta\kappa$ and $n > 1$ for λ. For the numerical results presented here, we use a dipole form factor $(n = 2)$ with a scale $\Lambda = 1$ TeV. The exponent $n = 2$ is chosen in order to suppress $W\gamma$ production at energies $\sqrt{\hat{s}} \gg \Lambda \gg M_W$, where novel phenomena such as resonance or multiple weak boson production are expected to become important.

III. PHENOMENOLOGICAL RESULTS

We shall now discuss the phenomenological implications of NLO QCD corrections to $W\gamma$ production at the Tevatron ($p\bar{p}$ collisions at $\sqrt{s} = 1.8$ TeV) and the SSC (pp collisions at $\sqrt{s} = 40$ TeV). We first briefly describe the input parameters, cuts, and the finite energy resolution smearing used to simulate detector response. We then discuss in detail the impact of NLO QCD corrections on the observability of nonstandard $WW\gamma$ couplings in $W\gamma$ production at the Tevatron and SSC. To simplify the dis-

cussion, we shall concentrate on $W^+\gamma$ production. In $p\bar{p}$ collisions the rates for $W^+\gamma$ and $W^-\gamma$ production are equal. At pp colliders, the $W^-\gamma$ cross section is slightly smaller than that of $W^+\gamma$ production. Furthermore, we shall only consider $W \to e\nu$ decays in the following. Since results and conclusions for $W\gamma$ production at the LHC are qualitatively very similar to those obtained for the SSC, we do not show differential distributions for LHC energies.

A. Input parameters

The numerical results presented in this section were obtained using the two-loop expression for α_s. The QCD scale Λ_{QCD} is specified for four flavors of quarks by the choice of parton distribution functions and is adjusted whenever a heavy quark threshold is crossed so that α_s is a continuous function of Q^2. The heavy quark masses were taken to be $m_b = 5$ GeV and $m_t = 150$ GeV. The SM parameters used in our numerical simulations are $M_Z = 91.173$ GeV, $M_W = 80.22$ GeV, $\alpha(M_W) = 1/128$, and $\sin^2\theta_W = 1 - (M_W/M_Z)^2$. These values are consistent with recent measurements at LEP, the CERN $p\bar{p}$ collider, and the Tevatron [33–35]. The soft and collinear cutoff parameters are fixed to $\delta_s = 10^{-2}$ and $\delta_c = 10^{-3}$ unless stated otherwise. The parton subprocesses have been summed over u, d, s, and c quarks and the Cabibbo mixing angle has been chosen such that $\cos^2\theta_C = 0.95$. The leptonic branching ratio has been taken to be $B(W \to e\nu) = 0.109$ and the total width of the W boson is $\Gamma_W = 2.12$ GeV. Except where otherwise stated, a single scale $Q^2 = M_{W\gamma}^2$, where $M_{W\gamma}$ is the invariant mass of the $W\gamma$ pair, has been used for the renormalization scale μ^2 and the factorization scale M^2.

In order to get consistent NLO results it is necessary to use parton distribution functions which have been fit to next-to-leading order. In our numerical simulations we have used the Martin-Roberts-Stirling (MRS) [36] set S0 distributions with $\Lambda_4 = 215$ MeV, which take into account the most recent New Muon Collaboration (NMC) [37] and Chicago-Columbia-Fermilab-Rochester (CCFR) Collaboration [38] data. The MRS distributions are defined in the universal ($\overline{\text{MS}}$) scheme and thus the factorization defining parameter λ_{FC} in Eqs. (3), (13), and (B2) should be $\lambda_{\text{FC}} = 0$. For convenience, the MRS set S0 distributions have also been used for the LO calculations.

B. Cuts

The cuts imposed in our numerical simulations are motivated by two factors: (1) the finite acceptance and resolution of the detector and (2) the need to suppress radiative W decay which results in the same final state as $W\gamma$ production. The finite acceptance of the detector is simulated by cuts on the four-vectors of the final-state particles. This group of cuts includes requirements on the transverse momentum of the photon and electron, and on the missing transverse momentum $\not{p}_T$ associated with the neutrino. Also included in this group are cuts

on the pseudorapidity η of the photon and electron. In addition, the electron and photon are also required to be separated in the pseudorapidity-azimuthal-angle plane

$$\Delta R(e,\gamma) = \left[\left(\Delta\phi_{e\gamma} \right)^2 + \left(\Delta\eta_{e\gamma} \right)^2 \right]^{1/2} . \qquad (24)$$

Since we ignore photon radiation from the final-state lepton line in our calculation, it is necessary to impose cuts which will efficiently suppress contributions from this diagram. In radiative W decays the lepton photon separation sharply peaks at small values due to the collinear singularity associated with the diagram in which the photon is radiated from the final-state lepton line. In the following we shall therefore impose a large separation cut of $\Delta R(e,\gamma) > 0.7$. Contributions from $W \to e\nu\gamma$ can be further reduced by a cluster transverse mass cut. In radiative W decays the $e\nu$ pair and the photon form a system with invariant mass $M(e\nu\gamma)$ close to M_W, whereas for $W\gamma$ production $M(e\nu\gamma)$ is always larger than M_W if finite W-width effects are ignored. This difference suggests that an $M(e\nu\gamma)$ cut can be used to separate $e\gamma \not{p}_T$ events originating from radiative W decays from $e\gamma \not{p}_T$ events originating from $W\gamma$ events. However, because of the nonobservation of the neutrino, $M(e\nu\gamma)$ cannot be determined unambiguously and the minimum invariant mass or the cluster transverse mass [39] is more useful:

$$M_T^2(e\gamma; \not{p}_T) = \left[\left(M_{e\gamma}^2 + |\mathbf{p}_T(\gamma) + \mathbf{p}_T(e)|^2 \right)^{1/2} + \not{p}_T \right]^2 - |\mathbf{p}_T(\gamma) + \mathbf{p}_T(e) + \not{\mathbf{p}}_T|^2 . \qquad (25)$$

Here $M_{e\gamma}$ denotes the invariant mass of the $e\gamma$ pair. For $W \to e\nu\gamma$ the cluster transverse mass peaks sharply at M_W [39] and drops rapidly above the W mass. Thus $e\gamma\not{p}_T$ events originating from $W\gamma$ production and radiative W decays can be distinguished if $M_T(e\gamma; \not{p}_T)$ is cut slightly above M_W (Ref. [5]). In our numerical results we thus require

$$M_T(e\gamma; \not{p}_T) > 90 \text{ GeV} . \qquad (26)$$

As shown in Ref. [11], this cut, together with the lepton photon separation cut, is quite efficient in suppressing radiative W decay events.

At leading order, $W\gamma$ events are produced not only by the Born subprocess $q_1\bar{q}_2 \to W\gamma$ but also by the photon bremsstrahlung process which proceeds via subprocesses such as $q_1 g \to W q_2$ followed by photon bremsstrahlung from the final-state quark. As demonstrated in Ref. [40], the bremsstrahlung process is not only significant, but is in fact the dominant production mechanism at supercollider center-of-mass energies. However, the bremsstrahlung process does not involve the $WW\gamma$ vertex and is thus a background to the Born process which is sensitive to the $WW\gamma$ coupling. Fortunately, the photon bremsstrahlung events can be suppressed by requiring the photon to be isolated [40]. A photon isolation cut typically requires the sum of the hadronic energy E_{had} in a cone of size R_0 about the direction of the photon to be less than a fraction ϵ_h of the photon energy E_γ, i.e.,

$$\sum_{\Delta R < R_0} E_{\text{had}} < \epsilon_h E_\gamma , \qquad (27)$$

with $\Delta R = [(\Delta\phi)^2 + (\Delta\eta)^2]^{1/2}$. To suppress the photon bremsstrahlung background, a photon isolation cut with $\epsilon_h = 0.15$ [41] and $R_0 = 0.7$ will be applied in the numerical results presented in this section. For this value of ϵ_h, the photon bremsstrahlung background is less than 10% of the Born $W\gamma$ signal rate.

The complete set of cuts can now be summarized as follows:

Tevatron	SSC
$p_T(\gamma) > 10$ GeV	$p_T(\gamma) > 100$ GeV
$p_T(e) > 20$ GeV	$p_T(e) > 25$ GeV
$\not{p}_T > 20$ GeV	$\not{p}_T > 50$ GeV
$|\eta(\gamma)| < 1.0$	$|\eta(\gamma)| < 2.5$
$|\eta(e)| < 2.5$	$|\eta(e)| < 3.0$
$\Delta R(e,\gamma) > 0.7$	$\Delta R(e,\gamma) > 0.7$
$M_T(e\gamma; \not{p}_T) > 90$ GeV	$M_T(e\gamma; \not{p}_T) > 90$ GeV
$\sum_{\Delta R < 0.7} E_h < 0.15 E_\gamma$	$\sum_{\Delta R < 0.7} E_h < 0.15 E_\gamma$

The effects of nonstandard $WW\gamma$ couplings are most pronounced in the central photon rapidity region. We therefore impose a rather stringent cut on $\eta(\gamma)$, in particular at the Tevatron. The large $p_T(\gamma)$ and $\not{p}_T$ cuts at SSC energies are chosen to reduce potentially dangerous backgrounds from $W + 1$ jet production, where the jet is misidentified as a photon, and from processes where particles outside the rapidity range covered by the detector contribute to the missing transverse momentum. Present studies [42, 43] indicate that these backgrounds are under control for $p_T(\gamma) > 100$ GeV and $\not{p}_T > 50$ GeV.

C. Finite-energy resolution effects

Uncertainties in the energy measurements of the charged lepton and the photon in the detector are simulated by Gaussian smearing of the particle four-momentum vector with standard deviation σ in our calculation. For distributions which require a jet definition, e.g., the $W\gamma + 1$ jet exclusive cross section, the jet four-momentum vector is also smeared. The standard deviation σ depends on the particle type and the detector. The numerical results presented here for the Tevatron and SSC center-of-mass energies were made using σ values based on the Collider Detector at Fermilab (CDF) and Solenoidal Detector Collaboration (SDC) specifications [44, 43].

D. Inclusive NLO cross sections

The sensitivity of $W\gamma$ production to anomalous $WW\gamma$ couplings in the Born approximation was studied in detail in Refs. [10] and [11]. The photon transverse momentum distribution, $d\sigma/dp_T(\gamma)$, the photon rapidity spectrum in the parton center-of-mass frame, $d\sigma/d|y_\gamma^*|$, and the $W\gamma$ invariant mass differential cross section $d\sigma/dM_{W\gamma}$ were found to be sensitive to the anomalous couplings. Of these three distributions, the $p_T(\gamma)$ distribution is the most sensitive indicator of anomalous couplings since it

is a directly observable quantity. On the other hand, the y_γ^* and $M_{W\gamma}$ distributions can only be reconstructed with a twofold ambiguity corresponding to the two solutions for the longitudinal momentum of the neutrino. Thus the sensitivity of these two distributions to anomalous couplings is degraded.

At hadron colliders the $W\gamma$ invariant mass cannot be determined unambiguously because the neutrino from

the W decay is not observed. If the transverse momentum of the neutrino is identified with the missing transverse momentum of a given $W\gamma$ event, the unobserved longitudinal neutrino momentum $p_L(\nu)$ can be reconstructed, albeit with a twofold ambiguity, by imposing the constraint that the neutrino and the charged lepton four-momenta combine to form the W rest mass [5, 45]. Neglecting the electron mass one finds

$$p_L(\nu) = \frac{1}{2\,p_T^2(e)} \left\{ p_L(e)(M_W^2 + 2\,\mathbf{p}_T(e)\cdot\slashed{\mathbf{p}}_T) \pm p(e)\left[(M_W^2 + 2\,\mathbf{p}_T(e)\cdot\slashed{\mathbf{p}}_T)^2 - 4\,p_T^2(e)\,\slashed{p}_T^2\right]^{1/2} \right\}, \tag{28}$$

where $p_L(e)$ denotes the longitudinal momentum of the electron. The two solutions for $p_L(\nu)$ are used to reconstruct two values for $M_{W\gamma}$ and y_γ^*. Both values are then histogrammed, each with half the event weight.

The dependence of the total cross section on the collinear and soft cutoff parameters is illustrated in Fig. 5 which shows the total NLO cross section for $pp \to W^+\gamma + X \to e^+\nu\gamma + X$ plotted versus δ_c and δ_s, for $\sqrt{s} = 40$ TeV and the cuts described in Sec. III B. The n- and $(n + 1)$-body contributions are also plotted for illustration ($n = 3$ for this process). The figure shows that the 3- and 4-body contributions, which separately have no physical meaning, vary strongly with δ_c and δ_s, however, the total cross section, which is the sum of the 3- and 4-body contributions, is independent of δ_c and δ_s over a wide range of these parameters.

The differential cross section for $p_T(\gamma)$ in the reaction $p\bar{p} \to W^+\gamma + X \to e^+\nu_e\gamma + X$ at $\sqrt{s} = 1.8$ TeV is shown in Fig. 6. The Born and NLO results are shown in Figs. 6(a) and 6(b), respectively. In both cases, results are displayed for the SM and for two sets of anomalous couplings, namely, $(\lambda_0 = 0.5, \Delta\kappa_0 = 0)$ and $(\lambda_0 = 0, \Delta\kappa_0 = 1.0)$. For simplicity, only one anomalous coupling at a time is allowed to differ from its SM value. The figure shows that at the Tevatron center-of-mass energy, NLO QCD corrections do not have a large influence on the sensitivity of the photon transverse momentum

distribution to anomalous couplings. Closer inspection reveals, however, that the shape of $d\sigma/dp_T(\gamma)$ is changed somewhat in the SM case, while it remains essentially unmodified for nonstandard couplings. The $O(\alpha_s)$ corrections at Tevatron energies are approximately 30% for the SM as well as for the anomalous coupling cases at small photon transverse momenta. In the SM case, the size of the QCD corrections increases to $\sim 60\%$ at large values of $p_T(\gamma)$, whereas they stay essentially at the 30% level for (sufficiently large) nonstandard $WW\gamma$ couplings. Since the anomalous terms in the helicity amplitudes grow like $\sqrt{\hat{s}}/M_W$ ($\hat{s}/M_W^2$) for $\Delta\kappa$ (λ), nonstandard couplings give large enhancements in the cross section at large values of $p_T(\gamma)$.

Figure 7 shows the reconstructed invariant mass distribution of the $W\gamma$ system for the same set of parameters as in the previous figure. The Born and NLO cross sections again display similar sensitivity to the effects of anomalous couplings. The shape change of the SM invariant mass distribution is less pronounced than in $d\sigma/dp_T(\gamma)$.

The size of the $O(\alpha_s)$ QCD corrections becomes more obvious in the photon rapidity distribution in the reconstructed parton center-of-mass frame, $d\sigma/d|y_\gamma^*|$, which is shown in Fig. 8. The parameters are again the same as in Fig. 6. The pronounced dip at $|y_\gamma^*| = 0$ in the SM case can be understood as a consequence of the radiation
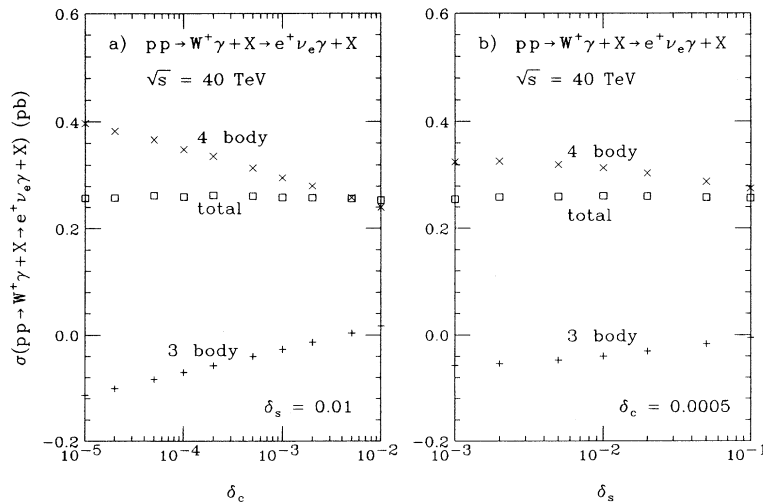

FIG. 5. Total cross section for $pp \to W^+\gamma + X \to e^+\nu_e\gamma + X$ at $\sqrt{s} = 40$ TeV; (a) vs δ_c and (b) vs δ_s. The 3- and 4-body contributions are also shown. The cuts imposed are summarized in Sec. III B.
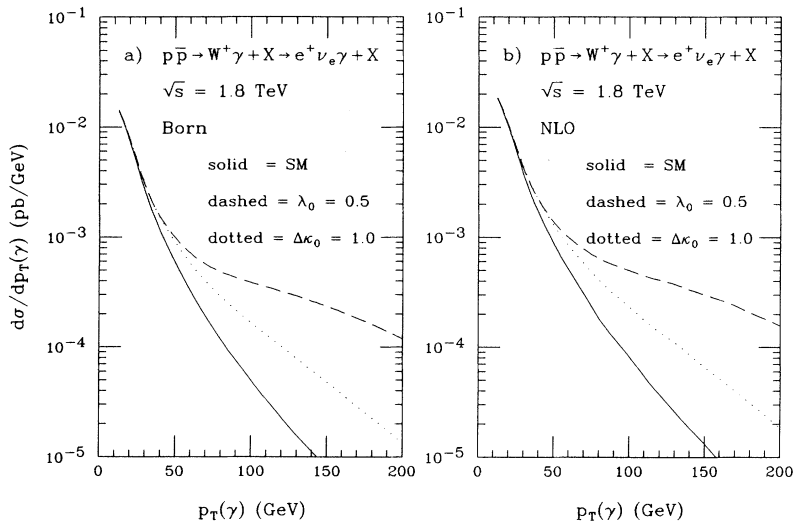
FIG. 6. The inclusive differential cross section for the photon transverse momentum in the reaction $p\bar{p} \to W^{+}\gamma + X \to e^{+}\nu_{e}\gamma + X$ at $\sqrt{s} = 1.8$ TeV; (a) in the Born approximation and (b) including NLO QCD corrections. The curves are for the SM (solid lines), $\lambda_{0} = 0.5$ (dashed lines), and $\Delta\kappa_{0} = 1.0$ (dotted lines). The cuts imposed are summarized in Sec. III B.

amplitude zero (RAZ). For $u\bar{d} \to W^{+}\gamma$ ($d\bar{u} \to W^{-}\gamma$) all contributing helicity amplitudes vanish for $\cos\Theta = -1/3$ ($+1/3$), where Θ is the angle between the quark and the photon in the parton center-of-mass frame. As a result, $d\sigma/d|y_{\gamma}^{*}|$ develops a dip at $|y_{\gamma}^{*}| = 0$. The inclusion of anomalous couplings at the $WW\gamma$ vertex destroys the RAZ and the dip is, at least partially, filled. Comparison of Figs. 8(a) and 8(b) shows that NLO QCD corrections and anomalous $WW\gamma$ couplings affect the $|y_{\gamma}^{*}|$ distribution in a qualitatively similar way. Next-to-leading log QCD corrections, however, do not completely obscure the dip at $|y_{\gamma}^{*}| = 0$. At Tevatron energies, the dominant contribution to the NLO cross section originates from quark-antiquark annihilation. Apart from the photon bremsstrahlung contribution, $\sigma_{\text{brem}}^{\text{NLO}}$ [see Eq. (12)], which is strongly suppressed by the photon isolation cut, Eq. (27), all $2 \to 2$ terms are proportional

to the $q_{1}\bar{q}_{2} \to W\gamma$ matrix element in the Born approximation and, therefore, preserve the radiation zero. Furthermore, the $2 \to 3$ process $q_{1}\bar{q}_{2} \to W^{\pm}\gamma g$ exhibits a RAZ at $\cos\Theta = \mp 1/3$ if the gluon is collinear with the photon [46], and also in the soft gluon limit, $E_{g} \to 0$.

The $p_{T}(\gamma)$ differential cross section, the reconstructed $W\gamma$ invariant mass distribution, and the $|y_{\gamma}^{*}|$ distribution for $W^{+}\gamma$ production at the SSC are shown in Figs. 9 – 11. Qualitatively similar results are also obtained for $W^{-}\gamma$ production. Results are shown for the SM (solid line) and for two sets of anomalous couplings, namely, ($\lambda_{0} = 0.25, \Delta\kappa_{0} = 0$) (dashed line) and ($\lambda_{0} = 0, \Delta\kappa_{0} = 1.0$) (dotted line). Because of the form factor parameters assumed, the result for $\Delta\kappa_{0} = 1$ approaches the SM result at large values of $p_{T}(\gamma)$ and $M_{W\gamma}$. As mentioned before, we have used $n = 2$ and a form factor scale of $\Lambda = 1$ TeV in all our numerical simulations [see Eqs. (22) and (23)].
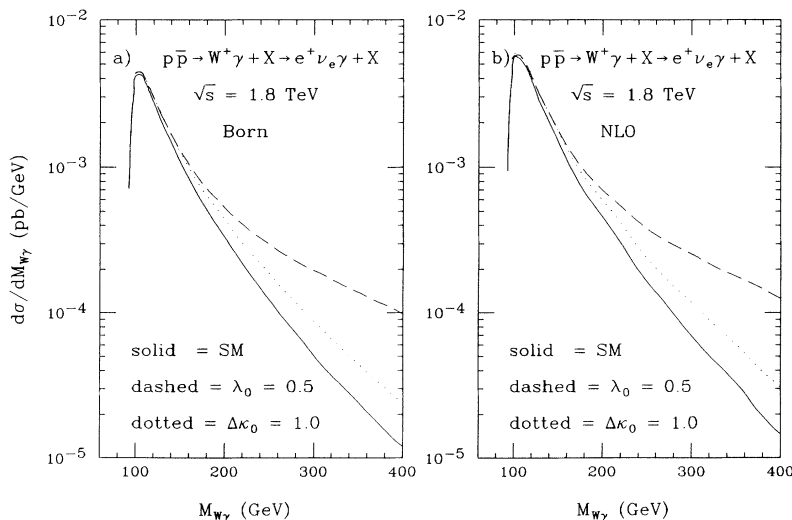

FIG. 7. The inclusive differential cross section for the reconstructed $W\gamma$ mass in the reaction $p\bar{p} \to W^{+}\gamma + X \to e^{+}\nu_{e}\gamma + X$ at $\sqrt{s} = 1.8$ TeV; (a) in the Born approximation and (b) including NLO QCD corrections. The curves are for the SM (solid lines), $\lambda_{0} = 0.5$ (dashed lines), and $\Delta\kappa_{0} = 1.0$ (dotted lines). The cuts imposed are summarized in Sec. III B.
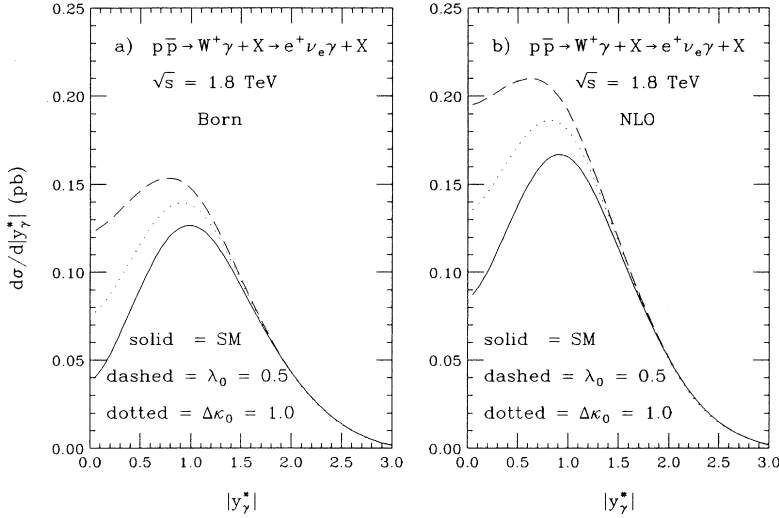
FIG. 8. The inclusive differential cross section for the photon rapidity in the reconstructed center-of-mass frame for the reaction $p\bar{p} \to W^+\gamma + X \to e^+\nu_e\gamma + X$ at $\sqrt{s} = 1.8$ TeV; (a) in the Born approximation and (b) including NLO QCD corrections. The curves are for the SM (solid lines), $\lambda_0 = 0.5$ (dashed lines), and $\Delta\kappa_0 = 1.0$ (dotted lines). The cuts imposed are summarized in Sec. III B.

For a larger scale Λ, the deviations from the SM result become more pronounced at high energies and transverse momenta (see Ref. [10] for details).

At SSC energies, the inclusive NLO QCD corrections are very large, most notably in the SM case. The shape of the $p_T(\gamma)$ distribution is significantly affected by the $O(\alpha_s)$ corrections. For $p_T(\gamma) = 1$ TeV, the QCD corrections increase the SM cross section by more than one order of magnitude. In the presence of anomalous couplings, the higher order QCD corrections are smaller than in the SM, although they are still large. Thus, at next-to-leading order, the sensitivity of the photon transverse momentum spectrum to anomalous couplings is severely reduced; the same is true, although to a smaller degree, for the $W\gamma$ invariant mass distribution (see Fig. 10). The low invariant mass tail in the NLO $M_{W\gamma}$ distribution is due to events where the W boson and the photon are almost collinear. The dip at $|y_\gamma^*| = 0$, indicating the radiation zero, is completely filled by the QCD corrections

(see Fig. 11). Note that the $|y_\gamma^*|$ distributions for the NLO SM and the $\Delta\kappa_0 = 1$ Born approximation are quite similar.

E. Exclusive NLO QCD corrections and jet veto

The size of the $O(\alpha_s)$ QCD corrections at supercollider energies and their effect on the shape of the $p_T(\gamma)$ distribution can be understood by considering the Born process $q_1\bar{q}_2 \to W\gamma$ and the quark gluon fusion process $q_1 g \to W\gamma q_2$ in more detail. In the SM, delicate cancellations between the amplitudes of the three Born diagrams shown in Fig. 1 occur in the central rapidity region. These cancellations are responsible for the radiation zero and suppress the $W\gamma$ differential cross section, in particular for large photon transverse momenta.

In the limit $p_T(\gamma) \gg M_W$, the cross section for $q_1 g \to W\gamma q_2$ can be obtained using the Altarelli-Parisi approximation for collinear emission. One finds
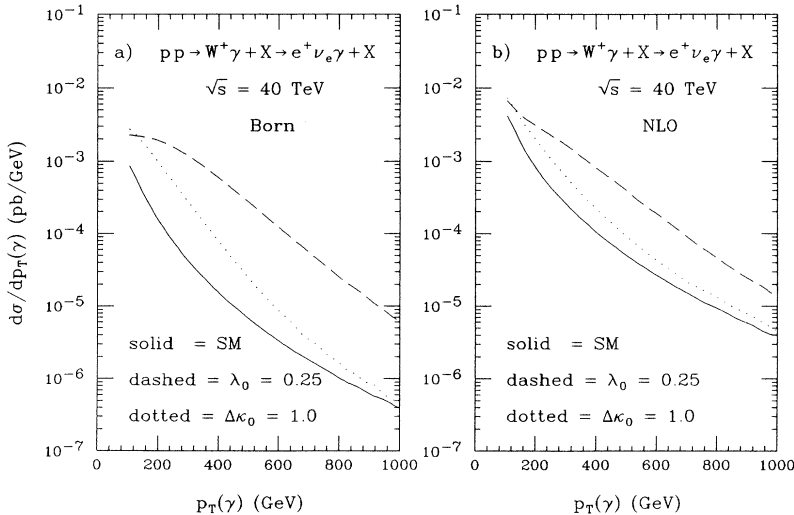

FIG. 9. The inclusive differential cross section for the photon transverse momentum in the reaction $pp \to W^+\gamma + X \to e^+\nu_e\gamma + X$ at $\sqrt{s} = 40$ TeV; (a) in the Born approximation and (b) including NLO QCD corrections. The curves are for the SM (solid lines), $\lambda_0 = 0.25$ (dashed lines), and $\Delta\kappa_0 = 1.0$ (dotted lines). The cuts imposed are summarized in Sec. III B.
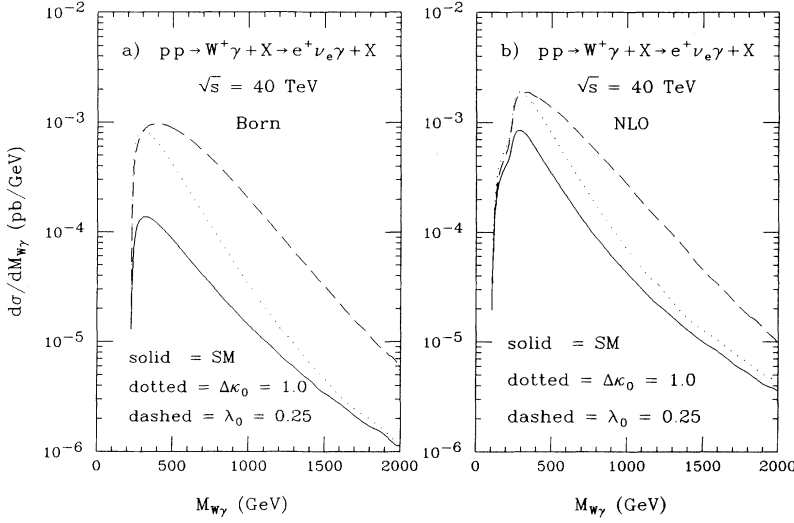
FIG. 10. The inclusive differential cross section for the reconstructed $W\gamma$ mass in the reaction $pp \rightarrow W^+\gamma + X \rightarrow e^+\nu_e\gamma + X$ at $\sqrt{s} = 40$ TeV; (a) in the Born approximation and (b) including NLO QCD corrections. The curves are for the SM (solid lines), $\lambda_0 = 0.25$ (dashed lines), and $\Delta\kappa_0 = 1.0$ (dotted lines). The cuts imposed are summarized in Sec. III B.

$$d\hat{\sigma}(q_1 g \rightarrow W\gamma q_2) = d\hat{\sigma}(q_1 g \rightarrow q_1\gamma) \frac{g_W^2}{16\pi^2} \ln^2\left(\frac{p_T^2(\gamma)}{M_W^2}\right),$$
(29)

where $g_W = e/\sin\theta_W$. Thus, the quark gluon fusion process carries an enhancement factor $\ln^2[p_T^2(\gamma)/M_W^2]$ at large photon transverse momentum. It arises from the kinematical region where the photon is produced at large p_T and recoils against the quark, which radiates a soft W boson which is almost collinear to the quark. Since the Feynman diagrams entering the derivation of Eq. (29) do not involve the $WW\gamma$ vertex, the logarithmic enhancement factor only affects the SM matrix elements. At the SSC, the $p_T(\gamma)$ differential cross section obtained using Eq. (29) agrees within 40% with the exact photon transverse momentum distribution for $p_T(\gamma) > 300$ GeV. Together with the very large qg luminosity at supercollider energies and the suppression of the SM $W\gamma$ rate at large photon transverse momenta in the Born approximation,

the logarithmic enhancement factor is responsible for the size of the inclusive NLO QCD corrections to $W\gamma$ production, as well as for the change in the shape of the $p_T(\gamma)$ distribution. The same enhancement factor also appears in the antiquark gluon fusion process, however, the $\bar{q}g$ luminosity is much smaller than the qg luminosity for large photon transverse momenta. Since the W does not couple directly to the gluon, the process $q_1\bar{q}_2 \rightarrow W\gamma g$ is not enhanced at large photon transverse momenta.

From the picture outlined in the previous paragraph, one expects that, to next-to-leading order at supercollider energies, $W\gamma$ events with a high p_T photon most of the time also contain a high transverse momentum jet. At the Tevatron, on the other hand, the fraction of high $p_T(\gamma)$ $W\gamma$ events with a hard jet should be considerably smaller, due to the much reduced qg luminosity at lower energies. For a given jet definition it is straightforward to split the inclusive NLO $W\gamma + X$ cross section into the NLO $W\gamma + 0$ jet and the leading order (LO) $W\gamma + 1$ jet cross sections. The decomposition of the
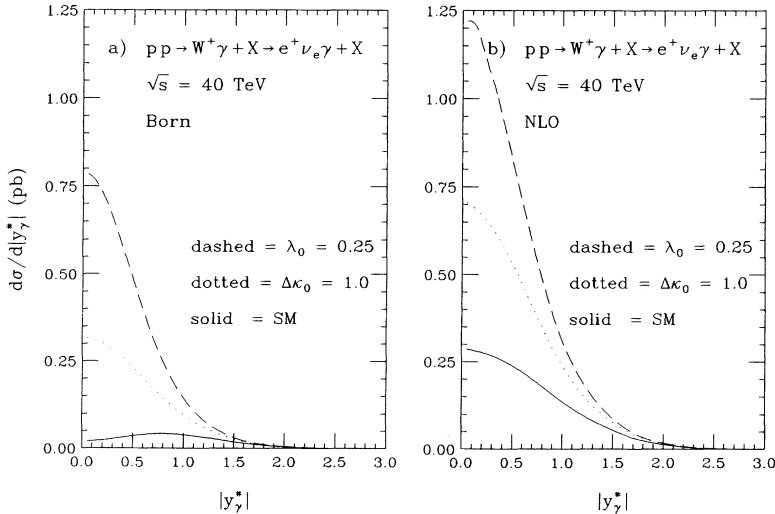

FIG. 11. The inclusive differential cross section for the photon rapidity in the reconstructed center-of-mass frame for the reaction $pp \rightarrow W^+\gamma + X \rightarrow e^+\nu_e\gamma + X$ at $\sqrt{s} = 40$ TeV; (a) in the Born approximation and (b) including NLO QCD corrections. The curves are for the SM (solid lines), $\lambda_0 = 0.25$ (dashed lines), and $\Delta\kappa_0 = 1.0$ (dotted lines). The cuts imposed are summarized in Sec. III B.
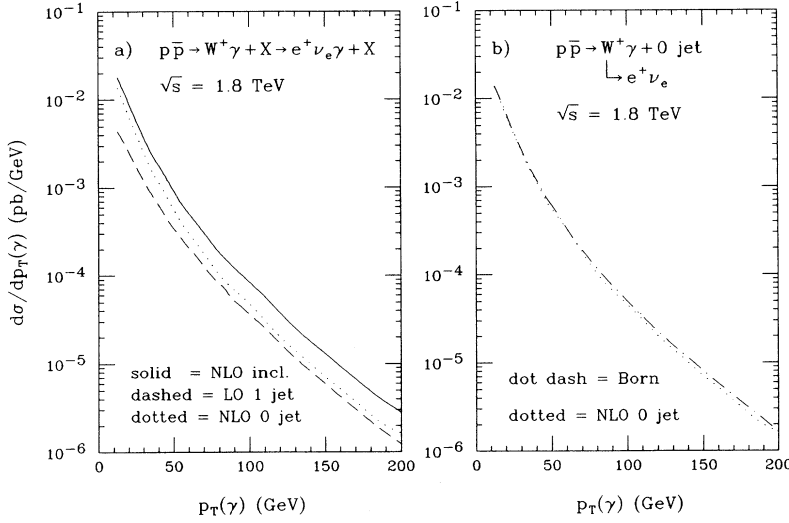
FIG. 12. The differential cross section for the photon transverse momentum in the reaction $p\bar{p} \to W^+\gamma \to e^+\nu_e\gamma$ at $\sqrt{s} = 1.8$ TeV in the SM. (a) The inclusive NLO differential cross section (solid line) is shown, together with the $O(\alpha_s)$ 0-jet (dotted line) and the (LO) 1-jet (dashed line) exclusive differential cross sections, using the jet definition in Eq. (30). (b) The NLO $W\gamma + 0$ jet exclusive differential cross section (dotted line) is compared with the Born differential cross section (dot-dashed line). The cuts imposed are summarized in Sec. III B.

inclusive SM NLO $p_T(\gamma)$ and $|y^*_\gamma|$ differential cross sections into NLO 0-jet and LO 1-jet exclusive cross sections at the Tevatron (SSC) are shown in Figs. 12(a) and 13(a) [Figs. 14(a) and 15(a)], respectively. The SM NLO 0-jet $p_T(\gamma)$ and $|y^*_\gamma|$ distributions at the Tevatron (SSC) are compared with the corresponding distributions obtained in the Born approximation in Figs. 12(b) and 13(b) [Figs. 14(b) and 15(b)]. Here, a jet is defined as a quark or gluon with

$$p_T(j) > 10 \text{ GeV} \quad \text{and} \quad |\eta(j)| < 2.5 \tag{30}$$

at the Tevatron, and

$$p_T(j) > 50 \text{ GeV} \quad \text{and} \quad |\eta(j)| < 3 \tag{31}$$

at the SSC. The sum of the NLO 0-jet and the LO 1-jet exclusive cross section is equal to the inclusive NLO cross section.

With the jet definition of Eq. (30), the inclusive NLO cross section at the Tevatron is composed predominately

of 0-jet events at low $p_T(\gamma)$ [see Fig. 12(a)]. Due to the logarithmic enhancement factor, the 1-jet cross section becomes relatively more important at large photon transverse momenta. For $p_T(\gamma)$ values above 100 GeV the 0-jet and 1-jet cross sections contribute nearly equally to the inclusive NLO cross section. Figure 12(b) compares the NLO $W\gamma + 0$ jet cross section with the result obtained in the Born approximation. The NLO and Born cross sections are almost equal at small $p_T(\gamma)$ for the jet definition used here. For large photon transverse momenta the NLO 0-jet result is about 20% smaller than the cross section in the Born approximation. It is obvious from Fig. 12 that the QCD corrections to the NLO 0-jet $p_T(\gamma)$ distribution are much smaller than the inclusive $O(\alpha_s)$ corrections.

The results shown in Fig. 12 were obtained for $Q^2 = M^2_{W\gamma}$. Since the $W\gamma + 1$ jet and the $W\gamma + 0$ jet cross section in the Born approximation are tree level results, the shape and the absolute normalization of the $p_T(\gamma)$ distributions are sensitive to the choice of the factoriza-
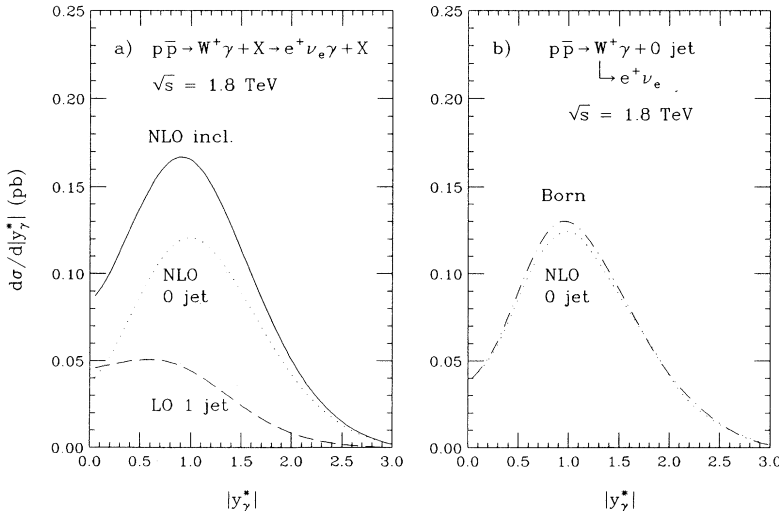

FIG. 13. The differential cross section for the photon rapidity in the reconstructed center-of-mass frame for the reaction $p\bar{p} \to W^+\gamma \to e^+\nu_e\gamma$ at $\sqrt{s} = 1.8$ TeV in the SM. (a) The inclusive NLO differential cross section (solid line) is shown, together with the $O(\alpha_s)$ 0-jet (dotted line) and the (LO) 1-jet (dashed line) exclusive differential cross sections, using the jet definition in Eq. (30). (b) The NLO $W\gamma + 0$ jet exclusive differential cross section (dotted line) is compared with the Born differential cross section (dot-dashed line). The cuts imposed are summarized in Sec. III B.
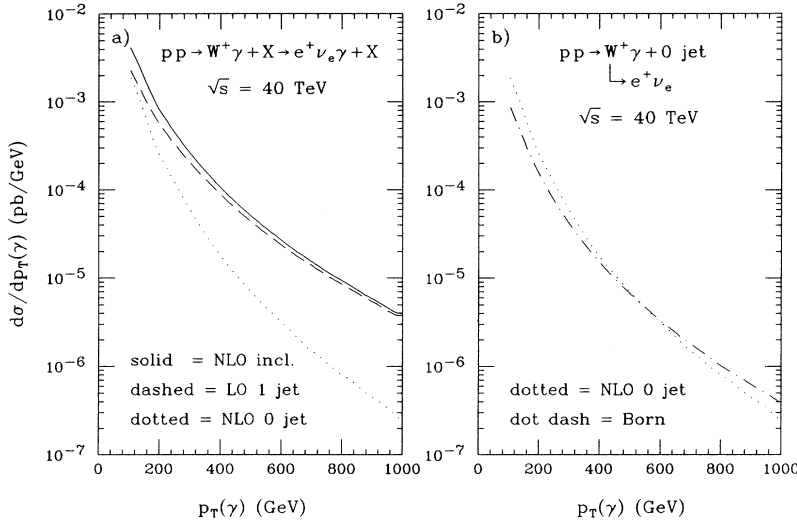
FIG. 14.   The differential cross section for the photon transverse momentum in the reaction $pp \to W^+\gamma \to e^+\nu_e\gamma$ at $\sqrt{s} = 40$ TeV in the SM. (a) The inclusive NLO differential cross section (solid line) is shown, together with the $O(\alpha_s)$ 0-jet (dotted line) and the (LO) 1-jet (dashed line) exclusive differential cross sections, using the jet definition in Eq. (31). (b) The NLO $W\gamma + 0$ jet exclusive differential cross section (dotted line) is compared with the Born differential cross section (dot-dashed line). The cuts imposed are summarized in Sec. III B.

tion scale Q^2. For $Q^2 = M_W^2$, for example, the $W\gamma + 1$ jet cross section is larger than the NLO $W\gamma + 0$ jet result for $p_T(\gamma) > 70$ GeV. The $p_T(\gamma)$ differential cross section in the Born approximation also changes its shape quite considerably. Whereas the result for $d\sigma/dp_T(\gamma)$ changes very little at small $p_T(\gamma)$, the differential cross section at $p_T(\gamma) = 200$ GeV for $Q^2 = M_W^2$ is about a factor 2 larger than the result for $Q^2 = M_{W\gamma}^2$. On the other hand, the NLO $W\gamma + 0$ jet photon p_T differential cross section is very insensitive to the value of Q^2 chosen. The Q^2 dependence of the $W\gamma$ cross section will be discussed in more detail later.

Figure 13(a) displays the inclusive NLO, the $O(\alpha_s)$ 0-jet, and the LO 1-jet $|y_\gamma^*|$ distributions for Tevatron energies. As we have observed earlier, the inclusive NLO QCD corrections partially fill in the dip at $|y_\gamma^*| = 0$ which signals the SM radiation zero. It is clear from Fig. 13(a) that events with a high p_T jet are responsible for this effect. The exclusive NLO 0-jet and Born $|y_\gamma^*|$ distributions are very similar, as demonstrated in Fig. 13(b). This is not surprising, since the contributions from the

$2 \to 3$ processes are suppressed in the 0-jet configuration. Apart from the photon bremsstrahlung term which contributes negligibly for the photon isolation cut we impose [see Eq. (27)], all $2 \to 2$ contributions preserve the radiation zero.

The decomposition of the inclusive NLO photon p_T distribution at the SSC into 0-jet and 1-jet fractions is shown in Fig. 14. For transverse momenta close to the minimum $p_T(\gamma)$ threshold, the 0-jet and 1-jet rates are approximately equal. At high $p_T(\gamma)$, the 1-jet cross section completely dominates. In Fig. 14(b), the NLO 0-jet photon p_T distribution is compared to the photon transverse momentum distribution in the Born approximation. Although the QCD corrections for $W\gamma + 0$ jet production are much smaller than in the inclusive reaction $pp \to W\gamma + X$, they are still sizable. At small p_T, the $O(\alpha_s)$ corrections to $W\gamma + 0$ jet production increase the cross section by about a factor 2 for the parameters used, whereas the QCD corrected cross section is somewhat smaller than the result obtained in the Born approximation at high photon transverse momenta.
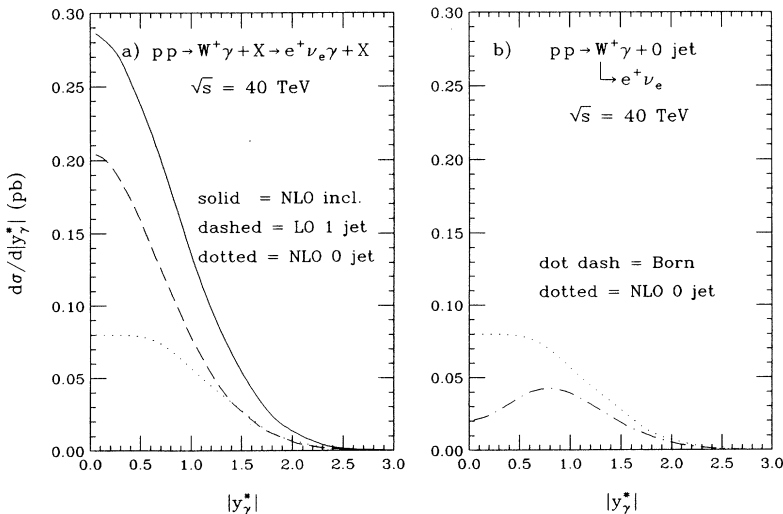

FIG. 15.   The differential cross section for the photon rapidity in the reconstructed center-of-mass frame for the reaction $pp \to W^+\gamma \to e^+\nu_e\gamma$ at $\sqrt{s} = 40$ TeV in the SM. (a) The inclusive NLO differential cross section (solid line) is shown, together with the $O(\alpha_s)$ 0-jet (dotted line) and the (LO) 1-jet (dashed line) exclusive differential cross sections, using the jet definition in Eq. (31). (b) The NLO $W\gamma + 0$ jet exclusive differential cross section (dotted line) is compared with the Born differential cross section (dot-dashed line). The cuts imposed are summarized in Sec. III B.

Figure 15(a) shows the inclusive NLO, the $O(\alpha_s)$ $W\gamma + 0$ jet, and the LO $W\gamma + 1$ jet $|y^*_\gamma|$ distributions for pp collisions at $\sqrt{s} = 40$ TeV. At small rapidities, the 1-jet channel contributes about 60% to the inclusive NLO cross section; for $|y^*_\gamma| \geq 1.4$ the 0-jet and 1-jet cross sections are approximately equal. In Fig. 15(b) we compare the NLO 0-jet result with the prediction obtained in the Born approximation. For the jet definition of Eq. (31), the QCD corrections to the $W\gamma + 0$ jet cross section completely fill the dip at $|y^*_\gamma| = 0$. For $|y^*_\gamma| \leq 0.7$, the NLO 0-jet cross section is almost completely flat. Even if the jet defining p_T threshold is reduced to 30 GeV, the radiation zero is still completely obscured by the QCD corrections. For the reduced p_T threshold, the NLO 0-jet $|y^*_\gamma|$ distribution almost coincides with the result obtained in the Born approximation for $|y^*_\gamma| > 1$ and is practically constant for $|y^*_\gamma| < 0.7$.

One of the motivations for performing NLO calculations is that the results often show a less dramatic dependence on the renormalization and factorization scale than the LO result. Figure 16 shows the scale dependence of the Born, the inclusive NLO, the $O(\alpha_s)$ 0-jet exclusive, and the 1-jet exclusive cross sections for the Tevatron, LHC, and SSC center-of-mass energies. To obtain the cross section at LHC energies, the same cuts and jet definition as for the SSC have been imposed. The total cross section for the reaction $p\overset{(-)}{p} \to W^+\gamma + X \to e^+\nu\gamma + X$ is plotted versus the scale Q. The factorization scale M^2 and the renormalization scale μ^2 have both been set equal to Q^2.

The scale dependence of the Born cross section enters only through the Q^2 dependence of the parton distribution functions. The qualitative differences between the results at the Tevatron and the supercolliders are due to the differences between $p\bar{p}$ versus pp scattering and the ranges of the x values probed. At the Tevatron, $W\gamma$ production in $p\bar{p}$ collisions is dominated by valence quark interactions. The valence quark distributions decrease slightly with Q^2 for the x values probed at the Tevatron. On the other hand, at the LHC and SSC, sea quark interactions dominate in the pp process and smaller x values

are probed. The sea quark distributions increase with Q^2 for the x values probed at the LHC and SSC. Thus the Born cross section decreases slightly with Q^2 at the Tevatron but increases with Q^2 at the LHC and SSC. The relative stability of the Born cross section at the Tevatron is accidental and depends on the cuts. For a larger $p_T(\gamma)$ cut, the Born cross section varies more strongly with Q.

The scale dependence of the 1-jet exclusive cross section enters via the parton distribution functions and the running coupling $\alpha_s(Q^2)$. Note that the 1-jet exclusive cross section is calculated only to lowest order and thus exhibits a considerable scale dependence. The dependence on Q here is dominated by the scale dependence of $\alpha_s(Q^2)$ which is a decreasing function of Q^2. At the NLO level, the Q dependence enters not only via the parton distribution functions and the running coupling $\alpha_s(Q^2)$, but also through explicit factorization scale dependence in the order $\alpha_s(Q^2)$ correction terms [see Eq. (13)]. The NLO 0-jet exclusive cross section is almost independent of the scale Q. Here, the scale dependence of the parton distribution functions is compensated by that of $\alpha_s(Q^2)$ and the explicit factorization scale dependence in the correction terms. The Q dependence of the inclusive NLO cross section is dominated by the 1-jet exclusive component and is significantly larger than that of the NLO 0-jet cross section. (The slight differences between the scale dependencies shown here and in Ref. [14] are due to the different cuts on the final state particles.)

The results obtained for the NLO exclusive $W\gamma + 0$ jet and the LO exclusive $W\gamma + 1$ jet differential cross sections depend explicitly on the jet definition. Only the inclusive NLO distributions are independent of the jet definition. The sensitivity of the NLO $W^+\gamma + 0$ jet differential cross section to the jet defining p_T threshold is investigated in Fig. 17(a) where we compare the photon transverse momentum distribution obtained in the Born approximation (solid line) with the $p_T(\gamma)$ spectrum of the NLO $W^+\gamma + 0$ jet process for two different jet definitions at the SSC. The dashed line shows the result obtained using the definition of Eq. (31). The dotted line displays the
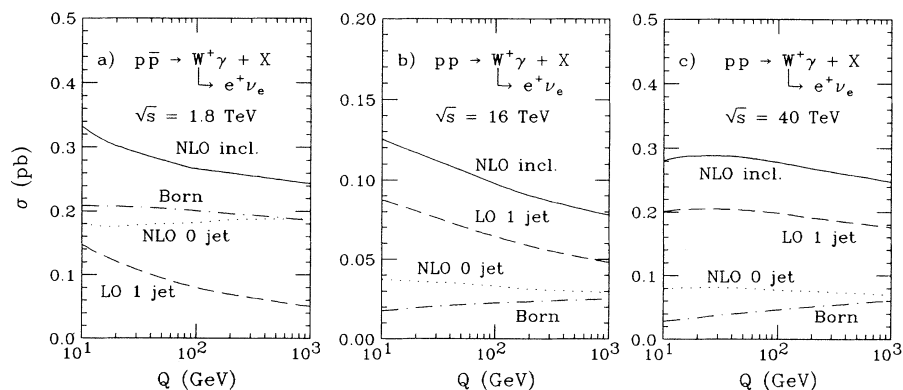

FIG. 16. The total cross section for $p\overset{(-)}{p} \to W^+\gamma + X \to e^+\nu_e\gamma + X$ in the SM vs the scale Q; (a) at the Tevatron, (b) at the LHC, and (c) at the SSC. The curves represent the inclusive NLO (solid lines), the Born (dot-dashed lines), the LO 1-jet exclusive (dashed lines), and the NLO 0-jet exclusive (dotted lines) cross sections. The cuts imposed are summarized in Sec. III B. For the jet definitions, we have used Eqs. (30) and (31).
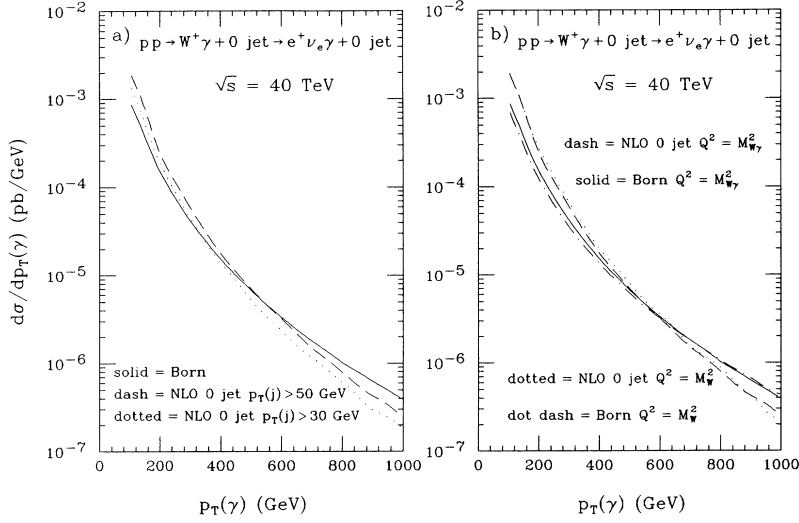
FIG. 17. The differential cross section for the photon transverse momentum in the reaction $pp \to W^+\gamma + 0$ jet $\to e^+\nu_e\gamma + 0$ jet at $\sqrt{s} = 40$ TeV in the SM. (a) Comparison of the result obtained in the Born approximation (solid line) with the NLO prediction for two different $p_T(j)$ thresholds. (b) Q^2 dependence of the $p_T(\gamma)$ distribution in the Born approximation (solid and dot-dashed line) and at next-to-leading order in α_s (dashed and dotted line). The cuts imposed are summarized in Sec. III B.

result if the $p_T(j)$ threshold is lowered to 30 GeV. In this case, the $p_T(\gamma)$ differential cross section is approximately 30% smaller than the result obtained for a 50 GeV $p_T(j)$ threshold. Present studies [43] suggest that jets with $p_T > 50$ GeV can be identified at the SSC without problems, whereas it will be difficult to reconstruct a jet with a transverse momentum smaller than about 30 GeV. The dashed and dotted lines in Fig. 17(a) therefore represent the typical uncertainties in the NLO $W\gamma + 0$ jet cross section originating from the jet definition at the SSC. Qualitatively similar results are obtained for the Tevatron. The jet transverse momentum threshold can also not be lowered to arbitrarily small values in our calculation for theoretical reasons. For transverse momenta below 5 GeV (20 GeV) at the Tevatron (SSC), soft gluon resummation effects are expected to significantly change the jet p_T distribution [47]. These effects are not included in our calculation.

In Fig. 16 we illustrated the dependence of the total cross section on the factorization and renormalization

scale Q. The total cross section, however, only poorly reflects the scale dependence of the differential cross section. In Fig. 17(b) we investigate the Q dependence of the $p_T(\gamma)$ differential cross section at the SSC for $W^+\gamma + 0$ jet production at NLO, using the jet definition of Eq. (31). Results are shown for $Q^2 = M_{W\gamma}^2$ (dashed line) and $Q^2 = M_W^2$ (dotted line). The result obtained for the NLO $W^+\gamma + 0$ jet $p_T(\gamma)$ distribution is almost independent of the scale over the whole range of $p_T(\gamma)$ shown. In contrast, the $p_T(\gamma)$ differential cross section obtained in the Born approximation displays a slight change in shape if Q^2 is changed from $M_{W\gamma}^2$ (solid line) to M_W^2 (dot-dashed line). The variation of the shape of the photon p_T distribution with Q^2 in the Born approximation is somewhat more pronounced at Tevatron energies.

The results shown in Figs. 12–15 suggest that the size of the $O(\alpha_s)$ QCD corrections can be significantly reduced by vetoing hard jets in the central rapidity region, i.e., by imposing a "zero jet" requirement and considering
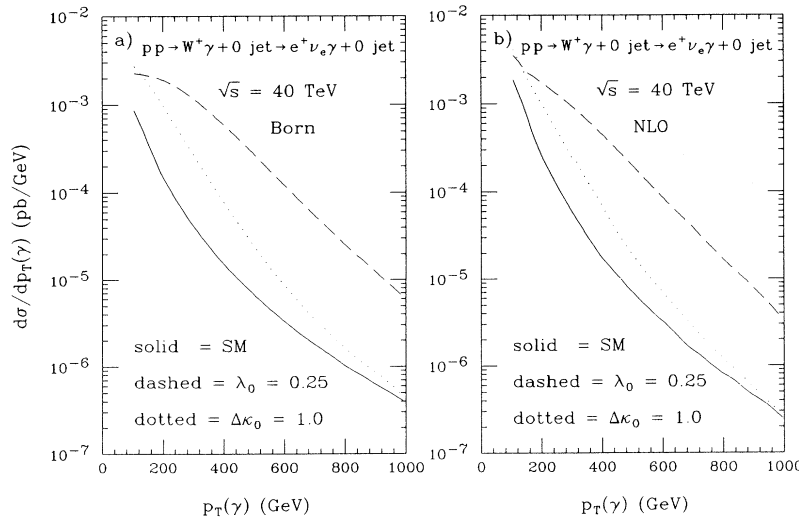
FIG. 18. The differential cross section for the photon transverse momentum for the exclusive reaction $pp \to W^+\gamma + 0$ jet $\to e^+\nu_e\gamma + 0$ jet at $\sqrt{s} = 40$ TeV; (a) in the Born approximation and (b) including NLO QCD corrections. The curves are for the SM (solid lines), $\lambda_0 = 0.25$ (dashed lines), and $\Delta\kappa_0 = 1.0$ (dotted lines). The cuts imposed are summarized in Sec. III B. For the jet definition, we have used Eq. (31).

the $W\gamma + 0$ jet channel only. A zero jet cut, for example, has been imposed in the CDF measurement of the ratio of W to Z cross sections [48] and the W mass measurement [49]. Figure 18 demonstrates that a jet veto to a large extent restores the sensitivity to anomalous $WW\gamma$ couplings lost in the inclusive NLO case at the SSC. Vetoing against jets with $p_T(j) > 50$ GeV and $|\eta(j)| < 3$, the $O(\alpha_s)$ QCD corrections affect the shape in the SM case, as well as for anomalous couplings, only modestly. For nonstandard $WW\gamma$ couplings, the shape is changed in a significant way for photon transverse momenta below 400 GeV only.

F. Sensitivity limits

As we have demonstrated so far, $O(\alpha_s)$ QCD corrections significantly affect $W\gamma$ production at hadron colliders and may reduce the sensitivity to anomalous $WW\gamma$ couplings substantially unless a jet veto is imposed. We now want to make this statement more quantitative by comparing the sensitivity limits for $\Delta\kappa_0$ and λ_0 achievable at the Tevatron and SSC for $W\gamma$ production in the Born approximation with the bounds obtained from the inclusive NLO $W\gamma + X$ and the exclusive NLO $W\gamma + 0$ jet calculation. To derive 1σ and 2σ (68% and 95% confidence level) limits we use the $p_T(\gamma)$ distribution and assume an integrated luminosity of 100 pb^{-1} at the Tevatron and 10^4 pb^{-1} at the SSC. In the Born approxima-

tion, the photon transverse momentum distribution in general yields the best sensitivity bounds. Furthermore, we use the cuts summarized in Sec. III B and the jet definitions in Eqs. (30) and (31). Only $W \to e\nu$ decays are taken into account in our analysis. To extract limits at the Tevatron, we shall sum over both W charges. For the SSC, we consider only $W^+\gamma$ production. Interference effects between $\Delta\kappa_0$ and λ_0 are fully incorporated in our analysis.

The statistical significance is calculated by splitting the $p_T(\gamma)$ distribution into 8 (5) bins at the SSC (Tevatron). In each bin the Poisson statistics are approximated by a Gaussian distribution. In order to achieve a sizable counting rate in each bin, all events with $p_T(\gamma) > 450$ GeV (30 GeV) at the SSC (Tevatron) are collected in a single bin. This guarantees that a high statistical significance cannot arise from a single event at large transverse momentum, where the SM predicts, say, only 0.01 events. In order to derive realistic limits we allow for a normalization uncertainty of 50% in the SM cross section. Background contributions are ignored in our derivation of sensitivity bounds.

Our results are summarized in Table I. The limits for $\Delta\kappa_0$ apply for arbitrary values of λ_0 and vice versa. At the Tevatron, QCD corrections only slightly influence the sensitivities which can be achieved with 100 pb^{-1}. The inclusive NLO $W^\pm\gamma + X$ and the exclusive NLO $W^\pm\gamma + 0$ jet limits are virtually identical. From the dis-

TABLE I. Sensitivities achievable at the 1σ and 2σ confidence levels (C.L.) for the anomalous $WW\gamma$ couplings $\Delta\kappa_0$ and λ_0 in $p\bar{p} \to W^\pm\gamma + X \to e^\pm\nu\gamma + X$ at the Tevatron and $pp \to W^+\gamma + X \to e^+\nu\gamma + X$ at the SSC. The limits for $\Delta\kappa_0$ apply for arbitrary values of λ_0 and vice versa. For the form factors we use Eqs. (22) and (23) with $n = 2$ and $\Lambda = 1$ TeV. We assume an integrated luminosity of 100 pb^{-1} at the Tevatron and 10^4 pb^{-1} at the SSC. The cuts summarized in Sec. III B are imposed. In the NLO 0-jet case we have used the jet definitions in Eqs. (30) and (31).

Coupling	C.L.	(a) Tevatron Born appr.	Incl. NLO	NLO 0-jet
$\Delta\kappa_0$	2σ	$+1.8$ -1.6	$+1.7$ -1.5	$+1.7$ -1.5
	1σ	$+1.1$ -0.8	$+1.0$ -0.8	$+1.0$ -0.8
λ_0	2σ	$+0.53$ -0.58	$+0.50$ -0.56	$+0.51$ -0.57
	1σ	$+0.29$ -0.35	$+0.27$ -0.34	$+0.28$ -0.34

Coupling	C.L.	(b) SSC Born appr.	Incl. NLO	NLO 0-jet
$\Delta\kappa_0$	2σ	$+0.33$ -0.34	$+0.46$ -0.59	$+0.37$ -0.39
	1σ	$+0.18$ -0.24	$+0.26$ -0.39	$+0.22$ -0.24
λ_0	2σ	$+0.033$ -0.029	$+0.044$ -0.053	$+0.033$ -0.035
	1σ	$+0.022$ -0.018	$+0.028$ -0.038	$+0.020$ -0.022

cussion in Secs. III D and III E one would expect that the sensitivity limits from the inclusive NLO $W^{\pm}\gamma + X$ cross section are somewhat worse than those obtained using the Born approximation. Table I shows that this is not the case. This result can be easily understood by noting that only about 11 events with $p_T(\gamma) > 30$ GeV are expected in the SM, including $O(\alpha_S)$ QCD corrections, for 100 pb^{-1}. Because of the small number of events, the reduced sensitivity to anomalous $WW\gamma$ couplings originating from the shape change induced by the $O(\alpha_s)$ corrections at large photon transverse momenta is not reflected in the bounds which can be achieved for the anomalous couplings. The slight improvement with respect to the limits obtained using the Born approximation is due to the increased cross section in the inclusive NLO case.

At SSC energies, the situation changes quite drastically. Inclusive NLO QCD corrections reduce the sensitivity to $\Delta\kappa_0$ (λ_0) by a factor ~ 1.7 (~ 2.1), although the inclusive $O(\alpha_s)$ corrections increase the total cross section by more than a factor 3. Furthermore, interference effects between the SM and anomalous terms in the helicity amplitudes considerably increase when inclusive NLO QCD corrections are taken into account. As a result, the bounds in the inclusive NLO case depend significantly on the sign of the anomalous coupling, in contrast to the limits obtained in the Born approximation. The increase of these interference effects is due to the logarithmic enhancement factor which is present in the SM quark-gluon fusion term at large photon transverse momenta.

A large portion of the sensitivity lost in the inclusive NLO case can be regained if a jet veto is imposed. The NLO $W^{+}\gamma + 0$ jet limits are typically 10–20 % weaker than those obtained in the Born approximation and depend only marginally on the jet definition criteria. In Sec. III E we found that the NLO $W\gamma + 0$ jet differential cross section is more stable to variations of the factorization scale Q^2 than the Born and inclusive NLO $W\gamma + X$ cross sections [see Figs. 16 and 17(a)]. The systematic errors which originate from the choice of Q^2 thus will be smaller for bounds derived from the NLO $W\gamma + 0$ jet differential cross section than those for limits obtained from the inclusive NLO $W\gamma + X$ or the Born cross section. Note that the results shown in Table I automatically imply that $W\gamma + 1$ jet production, with a high transverse momentum jet, will be less sensitive to anomalous $WW\gamma$ couplings than $W\gamma + 0$ jet production.

The bounds shown in Table I have been derived for a dipole form factor ($n = 2$) with a scale of $\Lambda = 1$ TeV. At Tevatron energies, the sensitivities achievable are insensitive to the exact form and the scale of the form factor (for $\Lambda > 400$ GeV). At the SSC, the situation is different and the sensitivity bounds depend significantly on the value chosen for Λ [10]. For $\Lambda = 5$ TeV, for example, the limits of Table I(b) improve by a factor ~ 2.5 (~ 2) for $\Delta\kappa_0$ (λ_0). The bounds in the inclusive NLO case are again weaker by up to a factor of 2 compared to those obtained in the Born approximation. If a jet veto is imposed, the sensitivities achievable are very similar to those found in the Born approximation. The usefulness of the zero jet requirement, thus, does not depend on details of the form factor assumed for the nonstandard $WW\gamma$ couplings.

In Table I, we have shown sensitivity limits only for the Tevatron and SSC. At LHC energies, the situation is very similar to that encountered at the SSC. For an integrated luminosity of 10^4 pb^{-1}, the sensitivities which can be achieved at the LHC are about a factor 1.5 worse than those expected for the SSC.

The bounds displayed in Table I are quite conservative. If $W \to \mu\nu$ decays and, at the SSC, $W^{-}\gamma + X$ production are included, the limits can easily be improved by 20–40 %. Further improvements may result from using more powerful statistical tools than the simple χ^2 test we performed. Our results, however, clearly demonstrate the advantage of a jet veto to probe the structure of the $WW\gamma$ vertex in $W\gamma$ production at hadron supercolliders.

IV. SUMMARY

$W\gamma$ production in hadronic collisions provides an opportunity to probe the structure of the $WW\gamma$ vertex in a direct and essentially model independent way. Previous studies of $p\overset{(-)}{p} \to W^{\pm}\gamma$ [10, 11] have been based on leading order calculations. In this paper we have presented an $O(\alpha_s)$ calculation of the reaction $p\overset{(-)}{p} \to W^{\pm}\gamma + X \to \ell^{\pm}\nu\gamma + X$ for general, CP conserving, $WW\gamma$ couplings, using a combination of analytic and Monte Carlo integration techniques. The $W \to \ell\nu$ decay has been included in the narrow width approximation in our calculation. In this approximation, diagrams in which the photon is radiated off the final-state lepton line are not necessary to maintain electromagnetic gauge invariance. For suitable cuts these diagrams can thus be ignored, which considerably simplifies the calculation. W decay spin correlations are correctly taken into account in our approach, except in the finite virtual contribution. The finite virtual correction term contributes only at the percent level to the total cross section and W decay spin correlations can thus be safely ignored here.

The photon p_T differential cross section is very sensitive to nonstandard $WW\gamma$ couplings. We found that QCD corrections significantly change the shape of this distribution. This shape change is due to a combination of destructive interference in the $W\gamma$ Born subprocess and a logarithmic enhancement factor in the qg and $\bar{q}g$ real emission subprocesses. The destructive interference suppresses the size of the $W\gamma$ Born cross section and is also responsible for the radiation amplitude zero. The logarithmic enhancement factor originates in the high $p_T(\gamma)$ region of phase space where the photon is balanced by a high p_T quark which radiates a soft W boson. The logarithmic enhancement factor and the large gluon density make the $O(\alpha_s)$ corrections large at high $p_T(\gamma)$, especially when the center of mass energy is large.

Since the Feynman diagrams responsible for the enhancement at large photon transverse momenta do not involve the $WW\gamma$ vertex, inclusive NLO QCD corrections to $W^{\pm}\gamma$ production tend to reduce the sensitivity to nonstandard couplings. At the Tevatron, for an integrated luminosity of 100 pb^{-1}, this effect is overwhelmed by the

increase in cross section induced by the QCD corrections. Because of the very large quark-gluon luminosity at the LHC and SSC, however, one expects that the sensitivity bounds which can be achieved at those machines are reduced by up to a factor 2 (see Table I).

The size of the QCD corrections at large photon transverse momenta may be reduced substantially and a large fraction of the sensitivity to anomalous $WW\gamma$ couplings which was lost at SSC and LHC energies may be regained by imposing a jet veto, i.e., by considering the exclusive $W\gamma + 0$ jet channel instead of inclusive $W\gamma + X$ production. Such a "zero-jet" requirement may be also very helpful to suppress the background from $t\bar{t}\gamma$ production [50] at the LHC and SSC. Furthermore, we found that the dependence of the NLO $W\gamma + 0$ jet cross section on the factorization scale Q^2 is significantly reduced compared to that of the inclusive NLO $W\gamma + X$ cross section. Uncertainties which originate from the variation of Q^2 thus will be smaller for sensitivity bounds obtained from the $W\gamma + 0$ jet channel than those for limits derived from the inclusive NLO $W\gamma + X$ cross section.

Although the magnitude of the QCD corrections at SSC energies is significantly reduced if a jet veto is imposed, the residual NLO corrections to $W\gamma + 0$ jet production are still quite large, in particular for small values of $p_T(\gamma)$, and cannot be ignored. This also means that in order to complete our understanding of QCD corrections in $W\gamma$ production, a full calculation of the $O(\alpha_s^2)$ corrections at SSC energies will be necessary. These corrections have recently been calculated in Ref. [7] in the soft-plus-virtual gluon approximation for CERN $p\bar{p}$ collider and Tevatron energies. Jet vetoing may also be useful to reduce the size of the $O(\alpha_s^2)$ corrections.

Our results show that NLO QCD corrections only slightly influence the sensitivity limits which can be achieved at the Tevatron. Nevertheless, it will be important to take these corrections into account when extracting information on the structure of the $WW\gamma$ vertex, in order to reduce systematic and theoretical errors. At the LHC and SSC it will be absolutely necessary to take into account the effects of higher order QCD corrections when experimental data and theoretical predictions for $W\gamma$ production are compared.

APPENDIX A: PHOTON BREMSSTRAHLUNG

The photon bremsstrahlung contribution to $W\gamma$ production and decay is calculated by convoluting the $O(\alpha_s)$ hard scattering subprocess cross section for W production and decay with the appropriate parton distribution and fragmentation functions:

$$\sigma_{\rm brem} = \sum_{a,b,c} \int G_{a/A}(x_a, M^2)\, G_{b/B}(x_b, M^2)\, D_{\gamma/c}(z_c, M^2)\frac{d\hat{\sigma}}{dv}(ab \to Wc \to \ell\nu c)\, dx_a\, dx_b\, dz_c\, dv \, . \tag{A1}$$

The squared matrix element for the subprocess $q_1(p_1) + \bar{q}_2(p_2) \to Wg \to \ell(p_3) + \nu(p_4) + g(p_5)$ is

$$\left|\mathcal{M}(q_1\bar{q}_2 \to Wg \to \ell\nu g)\right|^2 = \frac{2^9\,\pi^3\,\alpha_s\,\alpha^2}{x_W^2}\,\frac{s_{34}}{t_{15}t_{25}}\,\frac{\left[t_{14}^2 + t_{23}^2\right]}{\left[(s_{34} - M_W^2)^2 + (\Gamma_W M_W)^2\right]} \, , \tag{A2}$$

where $s_{ij} = (p_i + p_j)^2$, $t_{ij} = (p_i - p_j)^2$, and Γ_W is the total width of the W boson; spin and color averages are not included. The squared matrix elements for the subprocesses $q_1 g \to W q_2 \to \ell\nu q_2$ and $g\bar{q}_2 \to W\bar{q}_1 \to \ell\nu\bar{q}_1$ are obtained by crossing $p_2 \leftrightarrow -p_5$ and $p_1 \leftrightarrow -p_5$, respectively, and introducing an overall minus sign. If a photon isolation cut of the type discussed in Sec. III B is included, then the range of z is reduced from $0 \leq z \leq 1$ to $1/(1 + \epsilon_h) \leq z \leq 1$.

The LO bremsstrahlung cross section is obtained by using leading-log fragmentation functions. The numerical work in this paper was done using the parametrizations of Ref. [51] for the LO fragmentation functions:

$$zD_{\gamma/q}^{\rm LO}(z, Q^2) = F\left[\frac{Q_q^2(2.21 - 1.28z + 1.29z^2)z^{0.049}}{1 - 1.63\ln(1 - z)} + 0.0020(1 - z)^{2.0}z^{-1.54}\right], \tag{A3}$$

$$zD_{\gamma/g}^{\rm LO}(z, Q^2) = \frac{0.194}{8}\,F\,(1 - z)^{1.03}\,z^{-0.97}, \tag{A4}$$

where Q_q is the electric charge of the quark q (in units of the proton charge e), $F = (\alpha/2\pi)\ln(Q^2/\Lambda^2)$, and $\Lambda = \Lambda_4$. Since $\alpha_s(Q^2) = 12\pi/[(33 - 2N_F)\ln(Q^2/\Lambda^2)]$, these fragmentation functions are proportional to α/α_s.

The logarithmic growth of the fragmentation functions arises from an integration over the transverse momentum

of the photon with respect to the quark. The upper limit for this integration has been taken to be the typical hard scattering momentum scale Q^2. The divergence associated with the lower limit has been regulated by using the QCD scale parameter Λ as an infrared cutoff. Details on the derivation of these fragmentation functions can be found in Refs. [51, 52].

At the next-to-leading-order there are collinear singularities associated with final-state bremsstrahlung which must be factorized and absorbed into fragmentation functions. This will modify the leading-order quark fragmentation functions such that

$$D_{\gamma/q}^{\text{NLO}}(z) = D_{\gamma/q}^{\text{LO}}(z) + \frac{\alpha}{2\pi} Q_q^2 \left[\left\{ \frac{1+(1-z)^2}{z} \right\} \ln\left\{ z(1-z)\delta_c \frac{s_{12}}{M^2} \right\} + z \right] . \tag{A5}$$

Here δ_c is the collinear cutoff parameter and M^2 is the factorization scale. The new term is the remnant of the collinear singularity after the factorization process has been performed. The gluon fragmentation function is unchanged.

APPENDIX B: HARD COLLINEAR CORRECTIONS

The real emission processes, e.g., $q_1(p_1) + \bar{q}_2(p_2) \to W\gamma g \to \ell(p_3) + \nu(p_4) + \gamma(p_5) + g(p_6)$, have hard collinear singularities when $t_{16} \to 0$ or $t_{26} \to 0$. These singularities must be factorized and absorbed into the initial-state parton distribution functions. After the factorization is performed, the contribution from the remnants of the hard collinear singularities has the form

$$\sigma^{\text{HC}} = \sum_{q_1, \bar{q}_2} \int \frac{\alpha_s}{2\pi} \frac{d\hat{\sigma}^{\text{Born}}}{dv} (q_1\bar{q}_2 \to W\gamma \to \ell\nu\gamma) \, dv \, dx_1 \, dx_2$$

$$\times \left[G_{q_1/p}(x_1, M^2) \int_{x_2}^{1-\delta_s} \frac{dz}{z} G_{\bar{q}_2/p}^{(-)}\left(\frac{x_2}{z}, M^2\right) \tilde{P}_{qq}(z) + G_{q_1/p}(x_1, M^2) \int_{x_2}^{1} \frac{dz}{z} G_{g/p}\left(\frac{x_2}{z}, M^2\right) \tilde{P}_{qg}(z) \right.$$

$$\left. + G_{\bar{q}_2/p}^{(-)}(x_2, M^2) \int_{x_1}^{1-\delta_s} \frac{dz}{z} G_{q_1/p}\left(\frac{x_1}{z}, M^2\right) \tilde{P}_{qq}(z) + G_{\bar{q}_2/p}^{(-)}(x_2, M^2) \int_{x_1}^{1} \frac{dz}{z} G_{g/p}\left(\frac{x_1}{z}, M^2\right) \tilde{P}_{qg}(z) \right] , \tag{B1}$$

with

$$\tilde{P}_{ij}(z) \equiv P_{ij}(z) \ln\left(\frac{1-z}{z} \delta_c \frac{s_{12}}{M^2} \right) - P'_{ij}(z) - \lambda_{\text{FC}} \, F_{ij}(z) . \tag{B2}$$

The Altarelli-Parisi splitting functions in $N = 4 - 2\epsilon$ dimensions for $0 < z < 1$ are

$$P_{qq}(z, \epsilon) = C_F \left[\frac{1+z^2}{1-z} - \epsilon(1-z) \right] , \tag{B3}$$

$$P_{qg}(z, \epsilon) = \frac{1}{2(1-\epsilon)} \left[z^2 + (1-z)^2 - \epsilon \right] , \tag{B4}$$

and can be written

$$P_{ij}(z, \epsilon) = P_{ij}(z) + \epsilon P'_{ij}(z) , \tag{B5}$$

which defines the P'_{ij} functions. The functions F_{qq} and F_{qg} depend on the choice of factorization convention and the parameter λ_{FC} specifies the factorization convention; $\lambda_{\text{FC}} = 0$ for the universal ($\overline{\text{MS}}$ [18]) convention and

$\lambda_{\text{FC}} = 1$ for the physical (DIS) convention. For the physical convention the factorization functions are

$$F_{qq}(z) = C_F \left[\frac{1+z^2}{1-z} \ln\left(\frac{1-z}{z} \right) - \frac{3}{2} \frac{1}{1-z} + 2z + 3 \right] , \tag{B6}$$

$$F_{qg}(z) = \frac{1}{2} \left[\left\{ z^2 + (1-z)^2 \right\} \ln\left(\frac{1-z}{z} \right) + 8z(1-z) - 1 \right] . \tag{B7}$$

The transformation between the $\overline{\text{MS}}$ and DIS schemes is discussed in Ref. [53]. The parameter M^2 is the factorization scale which must be specified in the process of factorizing the collinear singularity. Basically, it determines how much of the collinear term is absorbed into the various parton distributions.

[1] R. W. Brown, K. O. Mikaelian, and D. Sahdev, Phys. Rev. D **20**, 1164 (1979); K. O. Mikaelian, M. A. Samuel, and D. Sahdev, Phys. Rev. Lett. **43**, 746 (1979).

[2] E. Eichten, I. Hinchliffe, K. Lane, and C. Quigg, Rev. Mod. Phys. **56**, 579 (1984); **58**, 1065(E) (1986).

[3] K. O. Mikaelian, Phys. Rev. D **17**, 750 (1978); K. O. Mikaelian, M. A. Samuel, and D. Sahdev, Phys. Rev. Lett. **43**, 746 (1979); R. W. Brown,

K. O. Mikaelian, and D. Sahdev, Phys. Rev. D **20**, 1164 (1979); T. R. Grose and K. O. Mikaelian, *ibid.* **23**, 123 (1981); S. J. Brodsky and R. W. Brown, Phys. Rev. Lett. **49**, 966 (1982); M. A. Samuel, Phys. Rev. D **27**, 2724 (1983); R. W. Brown, K. L. Kowalski, and S. J. Brodsky, *ibid.* **28**, 624 (1983); R. W. Brown and K. L. Kowalski, *ibid.* **29**, 2100 (1984).

[4] G. N. Valenzuela and J. Smith, Phys. Rev. D **31**, 2787 (1985).

[5] J. Cortes, K. Hagiwara, and F. Herzog, Nucl. Phys. **B278**, 26 (1986).

[6] J. Smith, D. Thomas, and W. L. van Neerven, Z. Phys. C **44**, 267 (1989).

[7] S. Mendoza, J. Smith, and W. L. van Neerven, Phys. Rev. D **47**, 3913 (1993).

[8] K. Hagiwara, R. D. Peccei, D. Zeppenfeld, and K. Hikasa, Nucl. Phys. **B282**, 253 (1987); D. Zeppenfeld, Phys. Lett. B **183**, 380 (1987); E. Yehudai, Phys. Rev. D **41**, 33 (1990); **44**, 3434 (1991); S. Y. Choi and F. Schrempp, Phys. Lett. B **272**, 149 (1991); S. Godfrey and K. A. Peterson, Report No. OCIP/C 92-7, 1992 (unpublished).

[9] U. Baur and D. Zeppenfeld, Nucl. Phys. **B325**, 253 (1989); U. Baur *et al.*, in *Proceedings of the ECFA Large Hadron Collider Workshop,* Aachen, Germany, 1990, edited by G. Jarlskog and D. Rein (CERN Report No. 90-10, Geneva, Switzerland, 1990), Vol. II, p. 956; U. Baur and M. A. Doncheski, Phys. Rev. D **46**, 1959 (1992).

[10] U. Baur and D. Zeppenfeld, Nucl. Phys. **B308**, 127 (1988).

[11] U. Baur and E. L. Berger, Phys. Rev. D **41**, 1476 (1990).

[12] H. Kuijf *et al.*, in *Proceedings of the ECFA Large Hadron Collider Workshop* [9], Vol. II, p. 91.

[13] UA2 Collaboration, J. Alitti *et al.*, Phys. Lett. B **277**, 194 (1992).

[14] J. Ohnemus, Phys. Rev. D **47**, 940 (1993).

[15] H. Baer, J. Ohnemus, and J. F. Owens, Phys. Rev. D **40**, 2844 (1989); H. Baer, J. Ohnemus, and J. F. Owens, *ibid.* **42**, 61 (1990); Phys. Lett. B **234**, 127 (1990); J. Ohnemus and J. F. Owens, Phys. Rev. D **43**, 3626 (1991); J. Ohnemus, *ibid.* **44**, 1403 (1991); **44**, 3477 (1991); H. Baer and M. H. Reno, *ibid.* **43**, 2892 (1991); B. Bailey, J. Ohnemus, and J. F. Owens, *ibid.* **46**, 2018 (1992); J. Ohnemus and W. J. Stirling, *ibid.* **47**, 2722 (1993); H. Baer, B. Bailey, and J. F. Owens, *ibid.* **47**, 2730 (1993); L. Bergmann, Ph.D. dissertation, Florida State University, Report No. FSU-HEP-890215, 1989 (unpublished).

[16] S. Frixione, P. Nason, and G. Ridolfi, Nucl. Phys. **B383**, 3 (1992).

[17] G. 't Hooft and M. Veltman, Nucl. Phys. **B44**, 189 (1972).

[18] W. A. Bardeen, A. J. Buras, D. W. Duke, and T. Muta, Phys. Rev. D **18**, 3998 (1978).

[19] U. Baur, E. W. N. Glover, and J. J. van der Bij, Nucl. Phys. **B318**, 106 (1989); V. Barger, T. Han, J. Ohnemus, and D. Zeppenfeld, Phys. Rev. D **41**, 2782 (1990).

[20] K. Hagiwara, R. D. Peccei, D. Zeppenfeld, and K. Hikasa, Nucl. Phys. **B282**, 253 (1987); U. Baur and D. Zeppenfeld, *ibid.* **B308**, 127 (1988); K. Gaemers and G. Gounaris, Z. Phys. C **1**, 259 (1979).

[21] A. De Rújula *et al.*, Nucl. Phys. **B384**, 31 (1992); P. Hernández and F. J. Vegas, Phys. Lett. B **307**, 116 (1993).

[22] C. Burgess and D. London, Phys. Rev. Lett. **69**, 3428 (1992); McGill Report No. 92/04 (unpublished); Phys.

Rev. D **48**, 4337 (1993).

[23] K. Hagiwara, S. Ishihara, R. Szalapski, and D. Zeppenfeld, Phys. Lett. B **283**, 353 (1992); Phys. Rev. D **48**, 2182 (1993).

[24] P. Méry, S. E. Moubarik, M. Perrottet, and F. M. Renard, Z. Phys. C **46**, 229 (1990); C. Arzt, M. Einhorn, and J. Wudka, Phys. Rev. D (to be published).

[25] D. Choudhury, P. Roy, and R. Sinha, Report No. TIFR-TH/93-08, 1993 (unpublished).

[26] M. E. Peskin and T. Takeuchi, Phys. Rev. Lett. **65**, 964 (1990); Phys. Rev. D **46**, 381 (1992).

[27] G. Altarelli and R. Barbieri, Phys. Lett. B **253**, 161 (1991); G. Altarelli, R. Barbieri, and S. Jadach, Nucl. Phys. **B369**, 3 (1992).

[28] A. Falk, M. Luke, and E. Simmons, Nucl. Phys. **B365**, 523 (1991); J. Bagger, S. Dawson, and G. Valencia, *ibid.* **B399**, 364 (1993).

[29] W. J. Marciano and A. Queijeiro, Phys. Rev. D **33**, 3449 (1986); F. Boudjema, K. Hagiwara, C. Hamzaoui, and K. Numata, *ibid.* **43**, 2223 (1991).

[30] J. A. M. Vermaseren, FORM User's Manual, NIKHEF-H, Amsterdam, 1989.

[31] J. M. Cornwall, D. N. Levin, and G. Tiktopoulos, Phys. Rev. Lett. **30**, 1268 (1973); Phys. Rev. D **10**, 1145 (1974); C. H. Llewellyn Smith, Phys. Lett. **46B**, 233 (1973); S. D. Joglekar, Ann. Phys. (N.Y.) **83**, 427 (1974).

[32] S. Willenbrock and D. Zeppenfeld, Phys. Rev. D **37**, 1775 (1988); U. Baur and D. Zeppenfeld, Phys. Lett. B **201**, 383 (1988).

[33] LEP Collaborations, D. Decamp *et al.*, Phys. Lett. B **276**, 247 (1992).

[34] D. Schaile, Z. Phys. C **54**, 387 (1992).

[35] UA2 Collaboration, J. Alitti *et al.*, Phys. Lett. B **241**, 150 (1990); CDF Collaboration, F. Abe *et al.*, Phys. Rev. Lett. **65**, 2243 (1990); Phys. Rev. D **43**, 2070 (1991); H. Plothow-Besch, Report No. CERN-PPE-90-168, 1990 (unpublished).

[36] A. D. Martin, R. G. Roberts, and W. J. Stirling, Phys. Rev. D **47**, 867 (1993).

[37] NMC, P. Amaudruz *et al.*, Phys. Lett. B **295**, 159 (1992).

[38] CCFR Collaboration, S. R. Mishra *et al.*, Report No. NEVIS-1459, 1992 (unpublished).

[39] V. Barger, A. D. Martin, and R. J. N. Phillips, Phys. Lett. **125B**, 339 (1983); E. L. Berger, D. DiBitonto, M. Jacob, and W. J. Stirling, *ibid.* **140B**, 259 (1984).

[40] J. Ohnemus and W. J. Stirling, Phys. Lett. B **298**, 230 (1993).

[41] P. Aurenche, R. Baier, and M. Fontannaz, Phys. Rev. D **42**, 1440 (1990); P. Aurenche *et al.*, in *Proceedings of the ECFA Large Hadron Collider Workshop* [9], Vol. II, p. 69; CDF Collaboration, F. Abe *et al.*, Phys. Rev. Lett. **68**, 2734 (1992).

[42] Y. Morita, in *Physics of the Superconducting Supercollider,* Proceedings of the Summer Study, Snowmass, Colorado, 1986, edited by R. Donaldson and J. Marx (Division of Particles and Fields of the APS, New York, 1987), p. 194; R. Zhu, Report No. CALT-68-1777, 1992 (unpublished); R. Zhu and H. Yamamoto, Report No. CALT-68-1802, 1992 (unpublished).

[43] SDC Collaboration, E. L. Berger *et al.*, SDC Technical Design Report, SDC-92-201, April 1992.

[44] CDF Collaboration, F. Abe *et al.*, Phys. Rev. D **45**, 3921 (1992).

[45] J. Stroughair and C. Bilchak, Z. Phys. C **26**, 415 (1984);

J. Gunion, Z. Kunszt, and M. Soldate, Phys. Lett. **163B**, 389 (1985); J. Gunion and M. Soldate, Phys. Rev. D **34**, 826 (1986); W. J. Stirling *et al.*, Phys. Lett. **163B**, 261 (1985).

[46] R. W. Brown, K. L. Kowalski, and S. J. Brodsky, Phys. Rev. D **28**, 624 (1983).

[47] T. Han, R. Meng, and J. Ohnemus, Nucl. Phys. **B384**, 59 (1992); P. Arnold and R. Kauffman, *ibid.* **B349**, 381 (1991); R. Kauffman, Phys. Rev. D **44**, 1415 (1991); **45**, 1512 (1992); C. P. Yuan, Phys. Lett. B **283**, 395 (1992).

[48] CDF Collaboration, F. Abe *et al.*, Phys. Rev. Lett. **64**, 152 (1990).

[49] CDF Collaboration, F. Abe *et al.*, Phys. Rev. Lett. **65**, 224 (1990); Phys. Rev. D **43**, 2070 (1991).

[50] E. Maina and S. Moretti, Phys. Lett. B **286**, 370 (1992).

[51] D. W. Duke and J. F. Owens, Phys. Rev. D **26**, 1600 (1982).

[52] J. F. Owens, Rev. Mod. Phys. **59**, 465 (1987).

[53] J. F. Owens and W. K. Tung, Annu. Rev. Nucl. Part. Sci. **42**, 291 (1992).